

# Addressing bedload flux variability due to grain shape effects and experimental channel geometry

Thomas Pächt,<sup>1†</sup> Yulan Chen,<sup>1</sup> Jiafeng Xie,<sup>1,2</sup> Rémi Monthiller,<sup>3</sup> Raphaël Maurin,<sup>4</sup> Katharina Tholen,<sup>5</sup> Yen-Cheng Lin,<sup>6</sup> Hao-Che Ho,<sup>6</sup> Peng Hu,<sup>1‡</sup> Zhiguo He,<sup>1¶</sup> and Orencio Durán Vinent<sup>7</sup>

<sup>1</sup>Institute of Port, Coastal and Offshore Engineering, Ocean College, Zhejiang University, 316021 Zhoushan, China

<sup>2</sup>State Key Laboratory of Fluid Power and Mechatronic Systems and Department of Engineering Mechanics, Zhejiang University, Hangzhou 310027, China

<sup>3</sup>Aix-Marseille University, CNRS, Centrale Marseille, Institut de Recherche sur les Phénomènes Hors Équilibre (IRPHÉ), Marseille 13384, France

<sup>4</sup>Université de Toulouse, Toulouse INP, CNRS, IMFT, 31400 Toulouse, France

<sup>5</sup>Institute for Theoretical Physics, Leipzig University, Postfach 100920, 04009 Leipzig, Germany

<sup>6</sup>Department of Civil Engineering, National Taiwan University, Taipei City 106, China

<sup>7</sup>Department of Ocean Engineering, Texas A&M University, College Station, Texas 77843-3136, USA

(Received xx; revised xx; accepted xx)

The study-to-study variability of bedload flux measurements in turbulent sediment transport borders an order of magnitude, even for idealized laboratory conditions. This uncertainty stems from physically poorly supported, empirical methods to account for channel geometry effects in the determination of the transport-driving bed shear stress and from study-to-study grain shape variations. Here, we derive a universal method of bed shear stress determination. It consists of a granular-physics-based definition of the bed surface and a channel sidewall correction based on linking Reynolds stress to bulk flow properties via Kolmogórov's theory of turbulence. Application of this method to bedload transport of spherical grains—to rule out grain shape effects—collapses data from existing laboratory measurements and grain-resolved CFD-DEM simulations for various channel geometries onto a single curve. In contrast, classical sidewall corrections, as well as an alternative bed surface definition, are unable to universally capture these data, especially those from shallow or very narrow channel flows. We then apply our method to an extended grain-shape-controlled data compilation, complemented by literature data for non-spherical grains and from grain-unresolved CFD-DEM simulations. This compilation covers a very diverse range of transport conditions, ranging from very narrow to infinitely wide channels, from shallow to deep channel flows, from mild to steep bed slopes, and from weak to intense transport. We generalize an existing physical bedload flux model to account for grain shape effects and show that it explains almost all the compiled data within a factor of only 1.3.

**Key words:**

† Email address for correspondence: 0012136@zju.edu.cn

‡ Email address for correspondence: pengphu@zju.edu.cn

¶ Email address for correspondence: hezhiguo@zju.edu.cn

## 1. Introduction

Bedload transport is a special kind of sediment transport in which typically coarse sedimentary grains roll, slide, and hop along the surface in response to the shearing of a loose granular bed by a flow of liquid. It plays a vital role in shaping the environments of Earth and other planetary bodies (Poggiali *et al.* 2016) by promoting the formation and growth of geological features of various scales, including ripples and dunes (Charru *et al.* 2013; Durán Vinent *et al.* 2019), deltas and fans (Baker *et al.* 2015), and laminations and cross-bedding (Schieber 2016; Shchepetkina *et al.* 2019). A key problem hampering our understanding of bedload-induced landscape evolution is the notoriously large noise commonly associated with measurements of the bedload flux, often exceeding an order of magnitude (Recking 2010; Ancey & Recking 2023). It partially originates from huge non-Gaussian flux fluctuations over large time scales, which even occur under steady flow conditions in the laboratory due to continuous topographic change (Dhont & Ancey 2018). However, also when restricted to steady flows over flat beds at short timescales, reported bedload fluxes can still substantially differ between laboratory studies for largely self-similar conditions, for both weak and intense transport-driving flows (Ancey & Recking 2023), and it has been unclear whether such differences arise due to physical or experimental reasons. On the one hand, physical reasons may come into play because dissimilarities in grain size and shape distributions are not accounted for by commonly used similarity parameters. On the other hand, study-to-study variability of the geometry of laboratory facilities is a potential culprit on the experimental side, especially in view of the associated large random and systematic uncertainties in the experimental determination of the transport-driving bed shear stress  $\tau_b$  (Yager *et al.* 2018). Focusing here on rectangular open channels, since they are geometrically similar to natural streams, the ratio  $b/h$  between the channel width  $b$  and flow depth  $h$  is a crucial parameter in this regard. Ideally, one would want  $b/h$  to be as large as possible to most closely resemble bedload transport in nature. However, in experimental reality,  $b/h$  is often of order unity, substantially weakening the shearing of the bed due to frictional losses at the sidewalls, causing the flow to be nonuniform in the cross-channel direction (Guo 2015). Another important parameter is the ratio between  $h$  and the grain diameter  $d$ . For shallow channel flows where  $h/d$  is close to unity, the method by which the bed surface elevation, and thus the flow depth  $h$  above it, is identified can have a large effect on the value of  $\tau_b$ .

To exemplify illustrate that channel geometry effects often are not appropriately accounted for, we choose two laboratory studies measuring bedload flux over a flat bed: Ni & Capart (2018), who conducted their experiments in a wide but shallow channel ( $h/d \sim 2-6$ ), and Deal *et al.* (2023), who used a very narrow but deep channel ( $b/h \approx 0.1$ ). Since the grains in both studies were spherical and relatively uniformly sized, one expects the same quantitative behavior of the nondimensionalized bedload flux  $Q_*$  as a function of the nondimensionalized bed shear stress or Shields number  $\Theta$  (Ancey 2020). However, when using these studies' reported values for  $\Theta$  and  $Q_*$ , based on their own definitions and methods to determine  $\tau_b$ , both datasets disagree from each other by a staggering factor of about 6 for  $\Theta \approx 0.2$  (figure 1). This indicates that at least one of them was inappropriately correcting for channel geometry effects, showcasing the need for a universal channel geometry correction method.

This study addresses two of the mentioned potential reasons for the study-to-study variability of laboratory bedload flux measurements: grain shape and channel geometry effects. We compile existing and new data of turbulent bedload transport along flat beds (no bedforms) of shape-controlled and (relatively) uniformly sized grains, obtained from

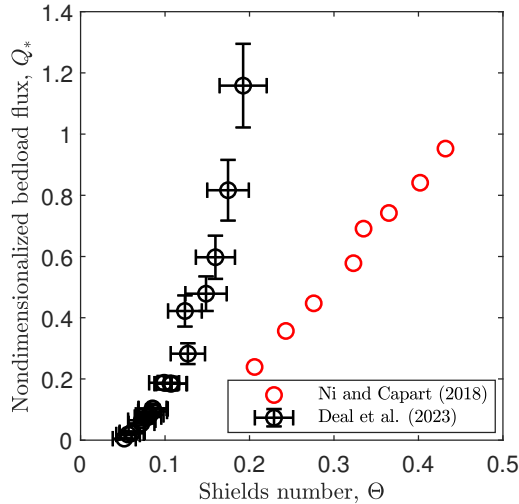


Figure 1: **Bedload flux measurements for spherical grains by Ni & Capart (2018) and Deal *et al.* (2023).** The Shields number  $\Theta$  and nondimensionalized bedload flux  $Q_*$  were defined and determined as described in these studies. For  $\Theta \approx 0.2$ , the values of  $Q_*$  disagree from each other by a factor of about 6.

experiments and grain-resolved (i.e., directly resolving fluid-particle interactions) and grain-unresolved numerical simulations based on various Computational Fluid Dynamics-Discrete Element Method (CFD-DEM) techniques, across channel flow widths and heights, grain shapes, bed slopes, and flow strengths. In §2, we reconcile channel geometry effects in these data through a universal sidewall correction, based on linking Reynolds stress to bulk flow properties via an extension of Kolmogórov’s theory of turbulence (Gioia & Bombardelli 2002; Gioia & Pinaki Chakraborty 2006), and a granular-physics-based definition to precisely determine the bed surface elevation (Pächt & Durán 2018*b*). This channel geometry correction method is validated, among others, through a collapse of experimental and grain-resolved numerical bedload flux data for spherical grains on a unique behavior, whereas classical methods (Einstein 1942; Johnson 1942; Guo 2015, 2017) yield very large scatter. Furthermore, in §3, we generalize an existing physical bedload flux model (Pächt & Durán 2020) to account for grain shape effects. It agrees with the entire channel-geometry-corrected data compilation within a factor of 1.3. The results are then discussed in §4 and conclusions are drawn in §5.

## 2. Universal channel geometry correction method

In this section, we derive and validate a universal channel geometry correction method to determine the transport-driving bed shear stress  $\tau_b$  for open channels with hydraulically rough sediment beds and hydraulically smooth sidewalls. We begin with the definition of  $\tau_b$  (§2.1) and derive from it, partially using known results, an expression that contains the flow depth  $h$  and the effective mixture sidewall shear stress  $\tau_w$  as unknowns. We then propose to determine  $h$  from an existing granular-physics-based definition of the bed surface elevation (§2.2) and derive an expression for  $\tau_w/\tau_b$  from an extension of Kolmogórov’s theory of turbulence (§2.3). In §2.4, the resulting channel geometry correction method is tested against a data compilation of turbulent bedload transport of spherical grains and other data.

### 2.1. Definition of bed shear stress

For turbulent bedload transport in open channels with hydraulically rough sediment beds, there is a limited region in the clear-water flow above the bedload layer where the streamwise ( $x$ ) fluid velocity profile  $u_x(z)$  approximately obeys the logarithmic law of the wall (Kidanemariam 2016; Jain *et al.* 2021; Deal *et al.* 2023):

$$u_x \simeq \frac{u_\tau}{\kappa} \ln \frac{z + z_o}{z_o}, \quad (2.1)$$

where  $\kappa = 0.41$  is the von Kármán constant,  $z$  the bed-normal coordinate, with  $z = 0$  the bed surface elevation,  $z_o$  the hydrodynamic roughness, which depends on both grain size and bedload flux (Durán *et al.* 2012), and  $u_\tau$  the friction velocity. The latter defines the bed shear stress  $\tau_b \equiv \rho_f u_\tau^2$ , where  $\rho_f$  is the fluid density. In what follows, we seek to express  $\tau_b$  in terms of known fluid and channel parameters.

Kidanemariam (2016) and Jain *et al.* (2021) conducted DNS-DEM simulations of bedload transport driven by negative streamwise fluid pressure gradients  $\chi$  at zero bed slope angle  $\alpha$  for infinitely wide and relatively deep channel flows. Both studies found that  $\tau_b$  defined via (2.1) is equivalent to the effective mixture shear stress evaluated at the bed surface,  $\sigma_{zx}(0)$ . Below, we generalize this result to open channels with sidewalls and arbitrary  $\alpha$ .

For a statistically steady ( $\partial_t = 0$ ) and streamwise uniform ( $\partial_x = 0$ ) open channel flow, the mixture momentum balance resulting from averaging over time  $t$  and the streamwise direction  $x$  reads (Pächt *et al.* 2026)

$$\partial_y \tilde{\rho} \tilde{u}_y \tilde{u}_x + \partial_z \tilde{\rho} \tilde{u}_z \tilde{u}_x = \partial_y \tilde{\sigma}_{yx} + \partial_z \tilde{\sigma}_{zx} + \chi + \tilde{\rho} g \sin \alpha, \quad (2.2)$$

where  $g$  is the gravitational acceleration,  $\tilde{\rho}$  the mixture density,  $\tilde{\mathbf{u}}$  the mixture velocity, and  $\tilde{\boldsymbol{\sigma}}$  the mixture shear stress tensor, which is composed of the averaged viscous fluid shear stress, the solid phase contact stress, a stress resulting from fluid-particle interactions, and the mixture Reynolds stress. Integrating (2.2) over height and the cross-channel coordinate  $y$ , written using the notations  $\langle \cdot \rangle_z \equiv \frac{1}{h} \int_0^h \cdot dz$  and  $\langle \cdot \rangle_y \equiv \frac{1}{b} \int_{-b/2}^{b/2} \cdot dy$ , then yields

$$-b \left[ \langle \tilde{\sigma}_{zx} - \tilde{\rho} \tilde{u}_z \tilde{u}_x \rangle_y \right]_{z=0}^{z=h} = h \left[ \langle \tilde{\sigma}_{yx} - \tilde{\rho} \tilde{u}_y \tilde{u}_x \rangle_z \right]_{y=-b/2}^{y=b/2} + bh\chi + bh \langle \langle \tilde{\rho} \rangle_y \rangle_z g \sin \alpha. \quad (2.3)$$

When assuming impermeable boundary conditions at the bed ( $\langle \tilde{\rho} \tilde{u}_z \rangle_y(0) = 0$ ) and free surface ( $\langle \tilde{\rho} \tilde{u}_z \rangle_y(h) = 0$ ) on average, then statistical steadiness and mass conservation would imply impermeable boundary conditions also at the sidewalls ( $\langle \tilde{\rho} \tilde{u}_y \rangle_z(\pm b/2) = 0$ ) on average, and vice versa. Although these boundaries are not necessarily perfectly impermeable, since low vertical transport may occur through the bed surface, we assume impermeability for simplicity, in which case the terms  $-\langle \tilde{\rho} \tilde{u}_z \tilde{u}_x \rangle_y(0, h)$  and  $-\langle \tilde{\rho} \tilde{u}_y \tilde{u}_x \rangle_z(\pm b/2)$  are Reynolds-like fluctuation stresses. We therefore identify  $\sigma_{zx} \equiv \langle \tilde{\sigma}_{zx} - \tilde{\rho} \tilde{u}_z \tilde{u}_x \rangle_y$ , when evaluated at  $z = 0$  or  $z = h$ , as the effective mixture bed and free-surface shear stresses, respectively, and  $\tau_w \equiv \mp \langle \tilde{\sigma}_{yx} - \tilde{\rho} \tilde{u}_y \tilde{u}_x \rangle_z(\pm b/2)$  as the effective mixture sidewall shear stress. Furthermore, we use the free-surface boundary condition  $\sigma_{zx}(h) = 0$  and the relation  $\langle \tilde{\rho} \rangle_y = (1 - \phi)\rho_f + \phi\rho_p$  (Pächt *et al.* 2026), where  $\rho_p$  is the particle density and  $\phi(z)$  the cross-channel-averaged particle volume fraction, and define the sediment transport load  $M \equiv \rho_p h \langle \phi \rangle_z$  (the average mass of transported grains—i.e., grains elevated above the bed surface—per unit area of the bed surface) and the vertical submerged gravitational acceleration  $\tilde{g}_z \equiv (1 - \rho_f/\rho_p)g \cos \alpha$ . Inserting these relations and definitions, and dividing by  $b$ , (2.3) becomes

$$\sigma_{zx}(0) = h(\chi + \rho_f g \sin \alpha) - (2h/b)\tau_w + M\tilde{g}_z \tan \alpha. \quad (2.4)$$

This expression is a generalization of the mixture balance by Bagnold (1956) to the case of a channel with sidewalls ( $h/b > 0$ ) and of the clear-water balance by Guo (2015) to the

case of a mixture ( $M > 0$ ); Guo (2015) also assumed  $\chi = 0$ . Since we later propose a Bagnoldian-type bedload transport model, we assume analogous to Bagnold (1956) that the bed shear stress defined via (2.1) is given by

$$\tau_b = \sigma_{zx}(0) - M\tilde{g}_z \tan \alpha. \quad (2.5)$$

This assumption is the generalization of the mentioned finding  $\tau_b = \sigma_{zx}(0)$  for  $\alpha = 0$  (Kidanemariam 2016; Jain *et al.* 2021). Note that the alternative assumption that  $\tau_b = \sigma_{zx}(0)$  for all  $\alpha$  would lead to substantial disagreement between the bedload transport model presented in §3.1 and the numerical data against which it is tested. Combining (2.4) and (2.5) yields

$$\tau_b = h(\chi + \rho_f g \sin \alpha) - (2h/b)\tau_w. \quad (2.6)$$

Here  $\tau_b$  depends on two unknowns: the bed surface elevation  $z = 0$  required to determine  $h$  and the effective mixture sidewall shear stress  $\tau_w$ . They are addressed below.

## 2.2. Definition of bed surface elevation

The water depth  $h$  is the average distance between the free-surface ( $z = h$ ) and bed surface ( $z = 0$ ) elevations. Many studies on bedload transport have treated  $h$  like it is a well-defined entity, without elaborating on what exactly they mean when referring to the bed surface (e.g., Deal *et al.* 2023). This nonspecificity is acceptable in situations where, regardless of the precise definition of the bed surface elevation  $z = 0$ , the resulting  $h$  is much larger than the grain size  $d$  (e.g., Deal *et al.* 2023). This is because distinct definitions of  $z = 0$  usually differ from one another only by a fraction of  $d$  and therefore yield only small uncertainty in the value of  $h$  for such deep channel flows due to  $h \gg d$ . However, for shallow channel flows, the situation is fundamentally different and a definition that accounts for the relevant grain scale characteristics and/or processes is required.

Most studies have defined  $z = 0$  via assuming that the relevant grain scale characteristics are the random close packing and near-stationarity of the granular bed underneath  $z = 0$ . For example,  $z = 0$  has been defined as the elevation where  $\phi$  is a constant proportion of the bed packing fraction (Durán *et al.* 2012; Rebai *et al.* 2022), via a yield criterion (Maurin *et al.* 2015), via critical values of the average particle velocity  $v_x$  (Rebai *et al.* 2022) or associated shear rate  $\dot{\gamma} = d_z v_x$  (Capart & Fraccarollo 2011), or a nearly diminishing bedload flux below  $z = 0$  (Ni & Capart 2018). However, since we later propose a Bagnoldian-type bedload transport model, we are more interested in a definition that accounts for the key assumptions behind such models.

Pächt & Durán (2018*b*) demonstrated that there are essentially three assumptions integral to Bagnoldian-type bedload transport models: (i) the vast majority of transport occurs above  $z > 0$ , (ii) the ratio  $\mu_b \equiv -\sigma_{zx}^p(0)/\sigma_{zz}^p(0)$  between the bed surface particle shear stress  $\sigma_{zx}^p(0)$  and surface particle pressure  $-\sigma_{zz}^p(0)$  is approximately constant, and (iii), except for intense transport conditions, the bed surface fluid shear stress  $\sigma_{zx}^f(0)$  reduces to approximately the threshold shear stress  $\tau_t$ . They argued that these assumptions are also expected to be satisfied for the flow-driven saltation of grains along a rigid, rough wall instead of a granular bed and therefore looked for a criterion that characterizes grain rebounds at a rough wall. From drawing an analogy to inclined granular flow, they hypothesized that, close to the wall,  $-\sigma_{zz}^p \dot{\gamma}$ , which describes the rate at which the granular flow converts mean particle kinetic energy density into solid phase Reynolds stress  $-\rho_p \phi v_z v_x$ , should peak. Translating this hypothesizes to sediment transport scenarios, they therefore defined the bed surface elevation through

$$\max(\dot{\gamma}\Sigma\phi) = (\dot{\gamma}\Sigma\phi)(0), \quad (2.7)$$

with  $\Sigma\phi(z) \equiv \int_z^h \phi(z')dz'$ , based on the approximation  $\sigma_{zz}^p \approx -\rho_p \Sigma\phi\tilde{g}_z$ . They found that in their coupled Reynolds-averaged Navier-Stokes (RANS)-DEM simulations of bedload transport (and windblown sand), when  $z = 0$  is defined through (2.7), it, indeed, approximately satisfies the three above assumptions across their simulated transport conditions.

### 2.3. Sidewall correction

Equation (2.6) is the same as that for clear-water flow (Guo 2015), except for generalized meanings of  $\tau_b$  and  $\tau_w$ . In particular, the bed shear stress  $\tau_b$ , even though it is based on the mixture flow above the bed surface, controls, like its clear-water counterpart, the slope of the logarithmic velocity profile in (2.1) (Kidanemariam 2016; Jain *et al.* 2021; Deal *et al.* 2023). Like previous studies on the sidewall correction for open channel flows with sediment transport (Einstein 1942; Johnson 1942; Vanoni & Brooks 1957; Guo 2015), we therefore model  $\tau_b$  and  $\tau_w$  as if the the flow above the bed surface were clear-water flow.

We start with rearranging (2.6) into the form

$$\tau_b = \frac{h(\chi + \rho_f g \sin \alpha)}{1 + \frac{2h}{b} f_w / f_b}, \quad (2.8)$$

where  $f_w \equiv \tau_w / (\rho_f U^2)$  and  $f_b \equiv \tau_b / (\rho_f U^2)$  are the friction factors associated with the sidewalls and bed surface, respectively, with  $U$  the bulk fluid flow velocity. The rougher these surfaces are, the larger is the rate at which the bulk flow energy density  $\rho_f U^2 / 2$  is frictionally dissipated, and the larger is the shear stress applied at them. The difficulty is now to relate the friction factor ratio  $f_w / f_b$  to bulk flow properties, such as the open channel flow geometry and  $U$ . In fact, one wants to avoid linking  $f_w / f_b$  to local flow properties, such the near-bed and near-sidewall flow velocity gradients, since they are usually not readily accessible.

A classical approach employed in numerous studies is to assume  $f_w = f_b$ , in which case  $\tau_b = \tau_R \equiv R(\langle \chi \rangle_z + \rho_f g \sin \alpha)$ , with  $R \equiv hb / (b + 2h)$  the hydraulic radius of the open channel (Guo 2015). This prediction is consistent with measurements of centerline flow velocity profiles in particle-free open channels consisting of only hydraulically smooth walls (sidewalls and bottom wall) for a large range of width-to-depth ratios ( $b/h = 1.04-9.5$ ) (Yang *et al.* 2005). However, in bedload transport, where the bed surface is typically hydraulically rougher than the hydraulically smooth sidewalls ( $f_b > f_w$ ),  $\tau_R$  merely constitutes a lower bound of  $\tau_b$ .

Another classical approach is the one by Einstein-Johnson (Einstein 1942; Johnson 1942; Vanoni & Brooks 1957; Guo 2017) (Appendix A), in which  $f_w$  is determined from the empirical Kármán-Prandtl law as the friction factor of a hydraulically fully smooth channel and then  $f_b$  linked to  $f_w$  via an *ad hoc* separation of the open channel into three parallel, non-interacting sidewall-free channels. However, this separation's only physical justification is its mathematically constructed consistency at the extreme limit  $f_b = f_w$ , where it rightfully predicts  $\tau_b = \tau_R$ .

Our approach presented below does not rely on Einstein's *ad hoc* channel separation but instead employs, for the Reynolds shear stress  $\tau_s$  at a given surface (the sidewalls or the bed surface), a relation based on Kolmogórov's theory of turbulence (Gioia & Bombardelli 2002; Gioia & Pinaki Chakraborty 2006):

$$\tau_s = -\rho_f \langle u'_{\parallel} u'_{\perp} \rangle = \kappa_{\tau} \rho_f U u_s, \quad (2.9)$$

where  $\langle \cdot \rangle$  denotes an averaging procedure and  $\kappa_{\tau}$  is a flow-geometry-dependent empirical coefficient. Equation (2.9) states that the surface-parallel velocity fluctuations  $u'_{\parallel}$  are dominated by the largest turbulent eddies in the system, whose characteristic velocity is  $U$ , whereas the surface-normal velocity fluctuations  $u'_{\perp}$  are primarily controlled by the largest normal

velocities  $u_s$  that turbulent eddies can generate near the surface. This relation, which was previously used to physically derive Manning's (Gioia & Bombardelli 2002) and Nikuradse's (Gioia & Pinaki Chakraborty 2006) empirical formulas, leads to  $f_w/f_b = u_w/u_b$ , where  $u_b$  and  $u_w$  are the values of  $u_s$  for the hydraulically rough bed surface and hydraulically smooth sidewalls, respectively.

One may question (2.9), since it assumes that the size of the eddies associated with the bed and those associated with the sidewalls are independent from each other. Einstein's sidewall correction exhibits an analogous characteristic, and Guo (2015) therefore challenged it by noting that it would produce a uniform shear stress on all boundaries,  $\tau_b = \tau_w = \tau_R$ , in hydraulically fully smooth or hydraulically fully rough channels, which should not be the case due to secondary flows. However, we reiterate that, for hydraulically fully smooth channels,  $\tau_b = \tau_R$  is well supported by measurements of centerline velocity profiles for a large range of width-to-depth ratios ( $b/h = 1.04\text{--}9.5$ ) (Yang *et al.* 2005), and we therefore believe that the assumption of independent eddy sizes is justified, at least in the context of determining  $\tau_b$ .

The sizes of the eddies governing  $u_b$  and  $u_w$  are controlled by the typical size  $r$  of the protrusion of bed surface grains (which roughly corresponds to the size of the largest eddies that fit into the cavities of the bed surface) and the thickness  $5(\kappa_\epsilon \kappa_u^3/2)^{-1/4} R \Re^{-3/4}$  of the viscous sublayer adjacent to the hydraulically smooth sidewalls (Gioia & Pinaki Chakraborty 2006), respectively, where  $\Re \equiv UR/\nu$  is the bulk flow Reynolds number, with  $\nu$  the kinematic fluid viscosity. Furthermore,  $\kappa_\epsilon = 5/4$  is a constant that follows from Kolmogórov's four-fifths law and  $\kappa_u \equiv u_R/U$  a parameter that relates the characteristic velocity  $u_R$  of the largest eddies to  $U$ . It is found to be largely insensitive to flow geometry, with  $\kappa_u = 0.036 \pm 0.005$  measured in pipe flow (Antonia & Pearson 2000) and  $\kappa_u = 0.033$  in the atmospheric boundary layer (Tennekes & Lumley 1972). With these parameters,  $f_w/f_b = u_w/u_b$  can be calculated via the smooth ( $f_w$ ) and rough ( $f_b$ ) limits of equation (2) of Gioia & Pinaki Chakraborty (2006) as

$$\frac{f_w}{f_b} = 2^{1/12} \frac{\sqrt{\Gamma_{-2/3}(\beta/5)} [\beta(\kappa_\epsilon \kappa_u^3)^{-1/4}]^{1/3} \Re^{-1/4}}{\sqrt{3/2}(r/R)^{1/3}} = c_{wb} \frac{\Re^{-1/4}}{(r/R)^{1/3}}, \quad (2.10)$$

where  $\Gamma_{-2/3}$  is the gamma function of order  $-2/3$ ,  $\beta = [3\Gamma(4/3)]^{3/4}$  the characteristic constant of the exponential decay of the velocity spectrum of turbulent flow, with  $\Gamma$  the gamma function, and  $c_{wb} \simeq 2.23$  is the scaling coefficient resulting from evaluating the expression in the middle of (2.10). Note that the prefactor  $2^{1/12}$  originates from the fact that  $R$  in Gioia & Pinaki Chakraborty (2006) refers to the pipe radius, which is twice the hydraulic radius  $R$  here. Since  $c_{wb}$  depends only on  $\kappa_\epsilon$ ,  $\kappa_u$ , and  $\beta$ , but not on the parameter  $\kappa_\tau$  defined through (2.9),  $c_{wb}$  is an approximately channel-geometry-independent parameter.

Equation (2.10) states that  $f_w/f_b$  is the ratio between the Blasius friction factor  $f_w \sim \Re^{-1/4}$  for hydraulically fully smooth channels and the friction factor  $f_b \sim (r/R)^{1/3}$  for hydraulically fully rough channels. Both scalings are of similar importance for the overall behavior of  $f_w/f_b$  and readily accessible for typical sediment transport datasets (e.g., see Table 1 for the values of  $\Re$  and  $R/r$  for the channels with sidewalls considered in this paper). They require knowledge of the bulk fluid flow velocity  $U$  and bed grain protrusion size  $r$ , respectively. We calculate  $U$  from the fluid discharge  $Q_f$  as (Rebai *et al.* 2022)

$$U = \frac{Q_f}{b \left( h - \int_0^h \phi dz \right)}. \quad (2.11)$$

Note that, except for intense bedload transport, the term  $\int_0^h \phi dz$  has only a marginal effect

Experimental or numerical study	Width-depth ratio, $b/h$	Friction factor ratio, $f_w/f_b$	Grain shape	Shape parameters			$\Re$	$s$	Hydrodynamic conditions				
				$S_f$	$C_D$	$\mu_s$			$Ga$	$\Theta$	$\alpha$	$h^*$	$R/r$
D23EXPs (Deal <i>et al.</i> 2023)	0.09–0.16	0.31–0.36	spheres	1	0.43	0.46	3760–6557	2.57	1334–1339	0.056–0.22	0.03–0.13	13–24	2.0
D23EXPe (Deal <i>et al.</i> 2023)	0.10–0.14	0.32–0.35	ellipsoids	0.83	0.60	0.60	4340–5553	2.42	1312–1314	0.071–0.16	0.03–0.09	15–22	2.0
D23EXPc (Deal <i>et al.</i> 2023)	0.10–0.13	0.36–0.39	chips	0.51	0.39	0.65	4258–5634	2.36	767–768	0.092–0.21	0.04–0.08	22–29	2.8
D23EXPg (Deal <i>et al.</i> 2023)	0.10–0.15	0.36–0.40	gravel	0.68	0.54	0.78	4135–6344	2.48	733–735	0.086–0.26	0.04–0.11	20–32	2.9–3.0
D23EXPP (Deal <i>et al.</i> 2023)	0.09–0.12	0.38–0.41	prisms	0.88	0.79	0.86	3769–4917	2.40	725	0.071–0.14	0.03–0.06	26–35	2.9–3.0
NC18EXP (Ni & Capart 2018)	5.2–7.5	0.39–0.42	spheres	1	0.49	0.45	4427–8568	1.39	998	0.12–0.21	0.02–0.03	2.3–3.3	3.6–4.8
R22EXPe (Rebai <i>et al.</i> 2022)	2.8–4.5	0.36–0.75	cylinders	0.84	0.32	0.60	3282–39287	1.42	738	0.25–1.06	0.05–0.06	8.7–14	12–16
R22EXPI (Rebai <i>et al.</i> 2022)	5.0–6.0	0.57–0.74	lenses	0.55	0.45	0.62	6110–16151	1.37	196	0.99–1.65	0.03–0.05	15–18	23–26
Z22LESn (Zhang <i>et al.</i> 2022)	0.13	0.29*	spheres	1	0.48	0.45	N/A	2.55	1354–1356	0.11–0.20	0.06–0.11	16–17	2.0
Z25LESn (Zhang <i>et al.</i> 2025)	0.12	0.29*	gravel	0.67	0.64	0.75	N/A	2.47	615–617	0.12–0.36	0.03–0.10	29	3.3
Z22LESw (Zhang <i>et al.</i> 2022)	$\infty$	N/A	spheres	1	0.48	0.45	N/A	2.55	1378	0.047–0.14	0.01–0.03	4.6–22	9.1–43
Z25LESw (Zhang <i>et al.</i> 2025)	$\infty$	N/A	gravel	0.67	0.64	0.75	N/A	2.47	617	0.18–0.29	0.01–0.014	29–30	59–60
J21DNS (Jain <i>et al.</i> 2021)	$\infty$	N/A	spheres	1	N/A	N/A	N/A	2.55	44.7	0.13	0 ( $\chi > 0$ )	18	36
KU17DNS	$\infty$	N/A	spheres	1	N/A	N/A	N/A	2.5	28.37	0.096–0.19	0 ( $\chi > 0$ )	13	26
M18RANS (Maurin <i>et al.</i> 2018)	$\infty$	N/A	spheres	1	0.42	0.40	N/A	1.75–4	1259–2521	0.11–1.38	0.01–0.19	2.0–62	4.0–123
M19RANSs (Monthiller 2019)	$\infty$	N/A	spheres	1	0.42	0.49	N/A	2.5	1782	0.16–0.72	0.05	4.1–18	8.3–37
M19RANSt1 (Monthiller 2019)	$\infty$	N/A	triplets	0.85	0.42	0.55	N/A	2.5	1782	0.24–1.01	0.05	6.1–26	12–51
M19RANSt2 (Monthiller 2019)	$\infty$	N/A	triplets	0.75	0.42	0.63	N/A	2.5	1782	0.31–1.28	0.05	8.0–33	16–65
M19RANSt3 (Monthiller 2019)	$\infty$	N/A	triplets	0.71	0.42	0.68	N/A	2.5	1782	0.39–1.57	0.05	9.9–40	20–80
M19RANSt4 (Monthiller 2019)	$\infty$	N/A	triplets	0.62	0.42	0.72	N/A	2.5	1782	0.47–1.86	0.05	12–47	24–95
M19RANSt5 (Monthiller 2019)	$\infty$	N/A	triplets	0.58	0.42	0.69	N/A	2.5	1782	0.56–2.18	0.05	14–55	28–111
LES	$\infty$	N/A	spheres	1	0.54	0.49	N/A	2.56	1341	0.14–0.32	0 ( $\chi > 0$ )	18–22	35–44
LESCD	$\infty$	N/A	spheres	1	1.78	0.49	N/A	2.56	1341	0.17–0.26	0 ( $\chi > 0$ )	20–23	40–47
BLRANS1	$\infty$	N/A	spheres	1	2.24	0.38	N/A	[1.1, 2.65]	50	0.044–1.21	0–0.16	$\infty$	$\infty$
BLRANS2	$\infty$	N/A	spheres	1	1.46	0.38	N/A	[1.1, 2.65]	100	0.058–1.21	0	$\infty$	$\infty$
BLRANSCD	$\infty$	N/A	spheres	1	15.9	0.38	N/A	2.65	50	0.063–0.45	0	$\infty$	$\infty$

Table 1: **Summary of bedload flux data shown in this study.** The top, middle, and bottom entries correspond to experiments, grain-resolved CFD-DEM simulations, and grain-unresolved CFD-DEM simulations, respectively. Those data of the datasets BLRANS1 and BLRANS2 with  $s = 2.65$  and  $\alpha = 0$  are from Pahzt & Duran (2020). The datasets Z25LESn and Z25LESw do not include data from simulations based on the “artificial-shrinkage method” by Zhang *et al.* (2025), since this method has been falsified (Chen *et al.* 2026). The asterisk \* indicates that the friction factor ratio  $f_w/f_b$  was not calculated but determined empirically. Note that the here listed parameter values of  $C_D$ ,  $Ga$ ,  $\Theta$ , and  $h^*$  are based on  $d = c_g$ .

on  $U$ . Hence, for the datasets by Deal *et al.* (2023), which will constitute a part of our data compilation and for which concentration profile data is not available, we calculate  $U$  as  $U \simeq Q_f / (bh)$ .

Furthermore, for random loose packed beds, like those in the classical experiments by Nikuradse (1933), where many bed surface grains protrude nearly fully into the flow,  $r$  is about equal to the physical roughness size (Gioia & Bombardelli 2002; Gioia & Pinaki Chakraborty 2006) and may be approximated as the volume-equivalent sphere diameter  $d_o \equiv \sqrt[3]{6V_p/\pi}$ , where  $V_p$  is the grain volume. However, in the context of bedload transport over mobile beds, the action of the flow smooths out and compactifies the bed surface (Allen & Kudrolli 2018; Cúñez *et al.* 2022), since flow-mobilized bed surface grains tend to resettle in more resistant bed pockets (Clark *et al.* 2017). As a result, the longer a bed is exposed to flow, the less do grains tend to protrude into it, and this process continues until a state of maximum resistance is reached (Pähtz *et al.* 2020). We estimate  $r$  in this state from laminar bedload experiments with spherical grains (Charru *et al.* 2004; Ouriemi *et al.* 2007; Houssais *et al.* 2015; Cúñez *et al.* 2022). They suggest that a Shields number  $\Theta \approx 0.1$  is needed to mobilize grains in the state of maximal resistance, which we use to infer the typical pivoting angle of grains resting in bed pockets as  $\psi \approx 60^\circ$  from figure 13 of Agudo *et al.* (2017). It corresponds to a protrusion of  $r = d \cos \psi \approx d/2$ .

Moreover, for non-spherical grains, we exploit that grains transported at elevations close to the bed surface tend to align their largest projected area parallel to the bed due to torque (Jain *et al.* 2020; Zhang *et al.* 2025). We therefore choose the shortest grain axis  $c_g$  as the parameter setting  $r$ . It complements the large ( $a_g$ ) and intermediate ( $b_g$ ) grain axes, defined through approximating grains as ellipsoids. Hence, we obtain  $r = c_g/2$  as an estimate for sediment transport applications. However, when comparing to data obtained from open-channel flow over manually prepared fixed beds (Song & Chiew 2001) or artificial surfaces (Auel *et al.* 2014), we use the standard  $r = d_o$  or  $r = k$ , respectively, where  $k$  is the measured physical roughness.

## 2.4. Validation of channel geometry correction method

### 2.4.1. Data compilation for turbulent bedload transport of spherical grains

In order to isolate channel geometry effects on bedload flux, we compile existing experimental datasets for *spherical grains*, assuming that grain shape effects are negligible for them. However, surprisingly, even though turbulent bedload transport has been studied for more than a century (Ancey 2020), flux measurements for spherical grains with a nearly uniform size distribution seem to be exceedingly scarce. (By contrast, such kind of measurements are the rule rather than exception when studying bedload transport driven by laminar flow (e.g., Ouriemi *et al.* 2007; Aussillous *et al.* 2013; Houssais *et al.* 2015; Cúñez *et al.* 2022).) After an extensive literature search, we have managed to find only a handful of datasets (Ni & Capart 2018; Frey *et al.* 2006; Frey 2014; Armanini & Cavedon 2019; Carrillo *et al.* 2022; Deal *et al.* 2023). Four of these were subsequently disregarded because of either partially crystallized beds and very large scatter (Frey *et al.* 2006; Frey 2014), or the presence of substantial suspended load in addition to bedload (Armanini & Cavedon 2019), or self-inconsistent data (Carrillo *et al.* 2022) (almost no bedload flux change with important variation of flow strength: increasing bed slope at constant flow depth). The only two remaining experimental datasets for spherical grains are those by Deal *et al.* (2023) and Ni & Capart (2018) discussed in the introduction. We therefore supplement the data compilation with additional datasets from numerical simulations that couple the DEM for the particle phase with a CFD method for the fluid phase that resolves the sub-grain scale: two datasets based on Direct Numerical Simulations (DNS) (Jain *et al.* 2021; Kidanemariam & Uhlmann 2017) for infinitely wide

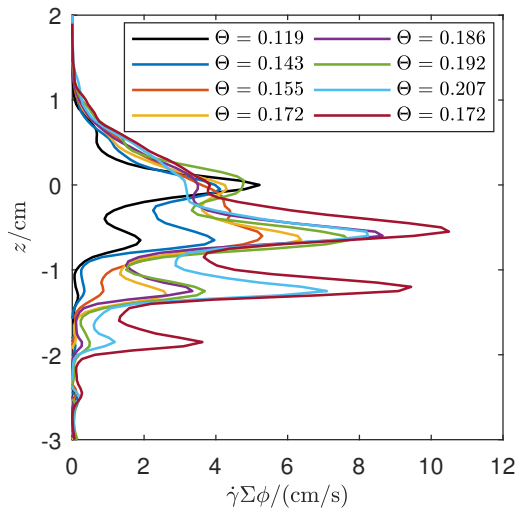


Figure 2: **Determination of bed surface elevation for experimental dataset NC18EXP (Ni & Capart 2018).** The vertical profiles of  $\dot{\gamma}\Sigma\phi$  exhibit several local maximums due to layering. We choose the top-most local maximum as the bed surface elevation, since the vertical profile of the fluid shear stress  $\sigma_{zx}^f(z)$  exhibits a focal point there,  $\sigma_{zx}^f(0) \approx \tau_t$  (§2.4.3), consistent with the theoretical expectation (Pächt & Durán 2018b).

channels ( $b/h = \infty$ , i.e., periodic boundaries) and two datasets based on grain-resolved Large Eddy Simulation (LES) (Zhang *et al.* 2022): one for  $b/h = \infty$  and one for a narrow-deep-channel configuration ( $b/h \approx 0.1$ ). Only such high-end methods, because they do not coarse-grain the particle phase and do not rely on empiricism for fluid-particle interactions, can be considered as similarly reliable as controlled experiments. The above spherical-grain datasets are denoted as D23EXPs, NC18EXP, Z22LESn, Z22LESw, J21DNS, and KU17DNS, and summarized in Table 1 together with other datasets used later. Note that, to Z22LESn and Z25LESn (used later), we are unable to apply our sidewall correction method, since the bulk flow velocity  $U$ , or data from which it can be inferred, was not reported. In addition, wall-modeled LES simulations such as these are known to underestimate the friction factors of channels with smooth walls (Nikitin *et al.* 2000; Yang *et al.* 2017), rendering (2.10) unusable. We therefore use the empirical sidewall correction that Zhang *et al.* (2025) applied to Z22LESn and Z25LESn,  $\tau_b = 3\tau_R$ , corresponding to  $f_w/f_b \approx 0.29$ , which is justified because it leads to an overlap with the sidewall-free simulations Z22LESw and Z25LESw, respectively, for otherwise almost the same conditions (Table 1).

For the spherical-grain datasets discussed in the previous paragraph, we determine the bed surface elevation using the method described in §2.2, provided the required data are available from the studies. This is the case for the dataset NC18EXP (figure 2), but not for D23EXPs, Z22LESn, Z22LESw, J21DNS, and KU17DNS. For the latter, we use the values reported in the respective studies. This approximation is justified for D23EXPs, Z22LESn, J21DNS, and KU17DNS, since  $h^* = h/d \gg 1$  (Table 1). In the case of Z22LESw, the authors of the respective study (Zhang *et al.* 2022) stated that they employed the method by Pächt & Durán (2018a) to calculate the bed surface elevation, which is the same as our method described in §2.2. For more details and the calculation of the bed shear stress uncertainty, see Appendix B.

#### 2.4.2. Test of channel geometry correction methods against data compilation

In this subsection, we test our and existing channel geometry correction methods against the spherical-grain data compilation discussed above. Once the bed shear stress  $\tau_b$  is determined

using a given channel geometry correction method, we are able to fully characterize the hydrodynamic bedload transport conditions by dimensionless similarity parameters. We choose the particle-fluid density ratio  $s \equiv \rho_p/\rho_f$ , Galileo number  $Ga \equiv d\sqrt{s\tilde{g}_z d}/\nu$ , Shields number  $\Theta \equiv \tau_b/(\rho_p\tilde{g}_z d)$ , dimensionless flow depth  $h^* \equiv h/d$ , and bed slope angle  $\alpha$  (Table 1). All spherical-grain datasets (and also those for non-spherical grains considered later) are well within the range of what is typically categorized as bedload transport ( $s \lesssim 10$  Pächt & Durán 2020), and most of them also satisfy  $s^{1/2}Ga \gtrsim 70$ , here termed “rough” transport conditions. In rough turbulent bedload, particle inertia dominate viscous fluid-particle interactions, and the nondimensionalized bedload flux  $Q_* \equiv Q/(\rho_p d\sqrt{s\tilde{g}_z d})$  is therefore expected to become essentially independent of  $s$  and  $Ga$  for sufficiently small  $\alpha$  (Pächt & Durán 2020; Ancy 2020; Zhang *et al.* 2022). We use this expectation as a tool to evaluate the different sidewall corrections outlined above (figure 3). It can be seen that the data for rough turbulent bedload transport of spherical grains, indeed, collapse, within measurement uncertainty, on a universal  $Q_*(\Theta)$ -behavior for our method (figure 3D), but do not collapse at all when employing a classical method or left uncorrected (figures 3A–3C), or when using our sidewall correction but a different bed surface definition (NC18EXP\* in figure 3D). Note that the spherical-grain dataset Z22LESn is not included in figure 3C, since the data for the bulk flow velocity  $U$ , required to calculate the Einstein-Johnson sidewall correction, are unavailable. Furthermore, Z22LESn in figure 3D is not based on our sidewall correction (since it also requires  $U$  as an input), but on the correction that Zhang *et al.* (2025) applied to this data set,  $\tau_b = 3\tau_R$ .

#### 2.4.3. Further independent tests of our channel geometry correction method

Figures 4A and 4B present further independent support for our sidewall correction. First, our correction predicts almost the same Shields numbers as those Deal *et al.* (2023) empirically determined as  $\tau_b = 2.41\tau_R$  via fitting (2.1) to their flow velocity data, both for spherical and non-spherical grains (figure 4A). Second, it is also consistent with experimental data from particle-free flows in open channels ( $b/h = 2.94\text{--}7.79$ ) consisting of hydraulically rough beds and hydraulically smooth sidewalls (Song 1994; Song & Chiew 2001; Auel *et al.* 2014) (figure 4B).

Furthermore, the strong quantitative difference between the spherical-grain data by Deal *et al.* (2023) and Ni & Capart (2018) discussed in the introduction (figure 1) is found to be predominantly the consequence of the latter authors’ bed surface definition (NC18EXP\* in figure 3D). In fact, figure 5 shows that the bed surface elevations resulting from their definition are much below ours. It can also be seen that the vertical profiles of the nondimensionalized local fluid shear stress  $\Theta_{z,x}^f$  for various flow strengths exhibit a focal point at the bed surface elevation ( $z = 0$ ) determined through our method, (2.7), with a focal value  $\Theta_{z,x}^f(0) \approx 0.04$  close to the transport threshold Shields number  $\Theta_t$ . As discussed in §2.2, the occurrence of such a focal point is precisely one of the properties we expect the bed surface to have.

### 3. Physical rough-bedload flux model across grain shapes, bed slopes, flow strengths and depths

In this section, we derive (§3.1) and validate (§3.3) a general bedload flux model. The validation makes use of an extended data compilation that complements the compilation for spherical grains, used in §2 to test channel geometry correction methods, with existing data from grain-shape-controlled experiments and grain-resolved CFD-DEM simulations for non-spherical grains, and with data for spherical and non-spherical grains from grain-unresolved CFD-DEM simulations (§3.2).

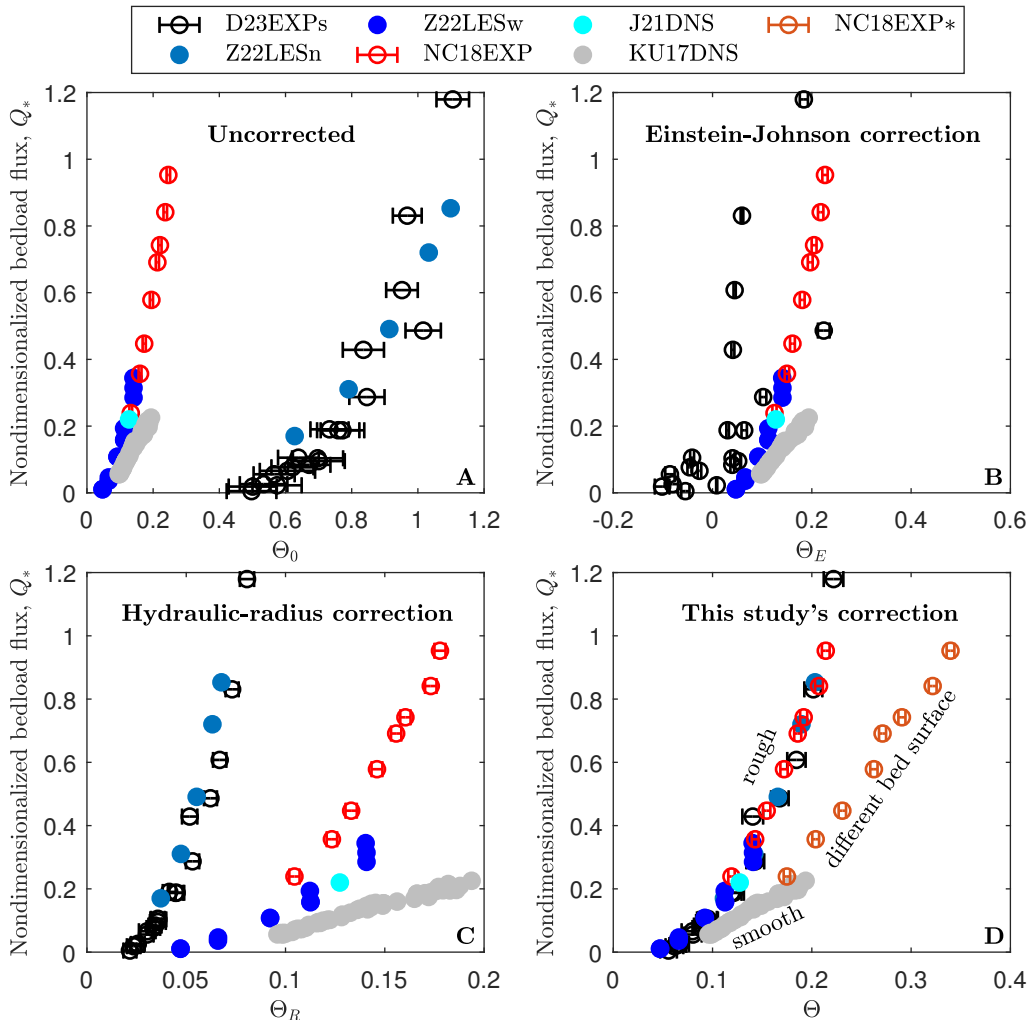


Figure 3: **Channel geometry corrections.** Nondimensionalized bedload flux  $Q_*$  versus Shields numbers for spherical grains: (A) uncorrected for sidewall effects ( $\Theta_0$ ), (B) hydraulic-radius correction (Guo 2015) ( $\Theta_R$ ), (C) Einstein-Johnson correction (Einstein 1942; Johnson 1942; Vanoni & Brooks 1957; Guo 2017) ( $\Theta_E$ ), (D) our universal correction ( $\Theta$ ). Symbols correspond to data from experiments and grain-resolved simulations (Table 1). An error bar indicates the standard error and/or uncertainty range.

In the absence of error bars, uncertainties are smaller than the symbol size. Except for KU17DNS ( $s^{1/2}Ga \approx 44.86$ , smooth), all data are in the rough transport regime ( $s^{1/2}Ga > 70$ ). The values of  $h$  used to determine  $\tau_b$  in Z22LESw and NC18EXP are based on a granular-physics-based bed surface definition (Pächt & Durán 2018b), (2.7), and in NC18EXP\* on the original definition reported by Ni & Capart (2018). For all other datasets, reported values of  $h$  are used as it has a negligible effect on the Shields numbers due to  $h \gg d$ . Z22LESn in D is not based on our sidewall correction, but on the correction that Zhang *et al.* (2025) applied to this data set,  $\Theta = 3\Theta_R$  (see text).

### 3.1. Model derivation

The model is derived in two steps. First, in §3.1.1, via generalizing an existing bedload flux model (Pächt & Durán 2020), we obtain an expression that predicts the nondimensionalized

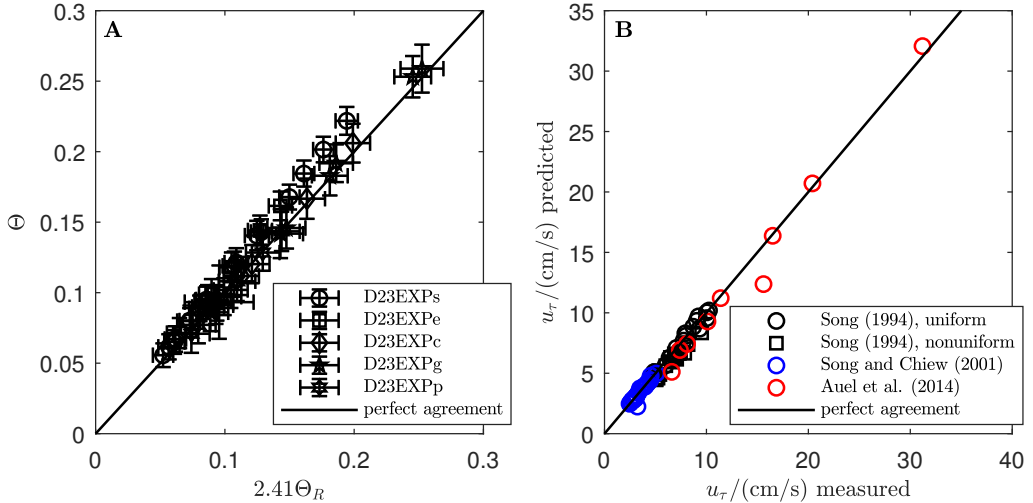


Figure 4: **Channel geometry corrections.** (A)  $\Theta$  versus  $2.41\Theta_R$  (using  $d = c_g$  for non-spherical-grain data, as explained in §3.1.1), based on  $\tau_b = 2.41\tau_R$ , the empirical correction in Deal *et al.* (2023). (B) Log-profile shear velocity  $u_\tau \approx \sqrt{\tau_b/\rho_f}$  predicted by our sidewall correction versus measured one for experimental data from particle-free flows in open channels consisting of hydraulically rough beds and hydraulically smooth sidewalls (Song 1994; Song & Chiew 2001; Auel *et al.* 2014) (data as summarized in the tables of Guo (2015)). For nonuniform flows, the bed slope  $\tan \alpha$  is corrected using equation (1b) of Guo (2015). The protrusion sizes are  $r = c_g/2$  for the experiments of Song (1994) (water-worked bed),  $r = d_o$  for those of Song & Chiew (2001) (sand grains glued on aluminum plate), and  $r = k$  for those of Auel *et al.* (2014) (with  $k$  the measured physical roughness).

bedload flux  $Q_*$  as a function of the excess Shields number  $\Theta - \Theta_t$ . Then, in §3.1.2, we explain how we calculate the unknown transport threshold  $\Theta_t$  appearing in this expression.

### 3.1.1. Bedload flux

Using a numerical model coupling the RANS equations with the DEM, Pächt & Durán (2020) simulated non-suspended sediment transport of spherical grains and derived a general transport rate expression holding for a large range of conditions, including turbulent bedload with  $s^{1/2}Ga \gtrsim 80$  and windblown sand:

$$Q_* = 2\kappa^{-1}\sqrt{\Theta_t}M_*(1 + c_M M_*), \quad (3.1)$$

with  $M_* \equiv M/(\rho_p d)$ . Based on the definition  $M \equiv \rho_p h \langle \phi \rangle_z$  of the transport load in §2.1,  $M_*$  can be interpreted as the number  $N$  of transported grains above a bed surface area of size  $\sim d^2$ . That is,  $M_*$  is a measure for the particle activity and therefore proportional to the excess Shields number  $\Theta - \Theta_t$  (Ancey 2020); the proportionality factor is derived shortly. Hence, for bedload transport, where  $1 + c_M M_* \approx 2\sqrt{c_M M_*}$  (arithmetic mean  $\approx$  geometric mean) is a good approximation as typically  $c_M M_* \sim O(1)$ , (3.1) predicts a bedload flux scaling similar to the classical formula by Meyer-Peter & Müller (1948).

In (3.1),  $2\kappa^{-1}\sqrt{\Theta_t}$  represents the dimensionless average particle velocity at  $\Theta_t$ , deduced from assuming that  $\Theta_t$  corresponds to the smallest Shields number at which a quasi-continuous hopping-rebound motion (saltation) of a test grain along a stationary bed in a grain-motion-undisturbed logarithmic fluid velocity profile can be sustained, a so-called “rebound threshold” (Pächt *et al.* 2020). Furthermore, the term  $c_M M_*$ , with  $c_M = 1.7$  a constant parameter determined from the simulations, encodes the rate of collisions between

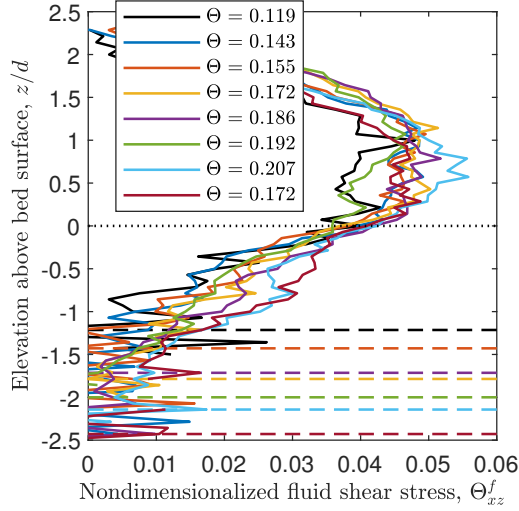


**Figure 5: Independent evidence supporting our bed surface elevation definition.**

Vertical profiles (solid lines) of the nondimensionalized fluid shear stress  $\Theta_{zx}^f \equiv \sigma_{zx}^f / (\rho_p \tilde{g}_z d)$  for the dataset NC18EXP (Ni & Capart 2018). The data exhibit a focal point at the bed surface elevation  $z = 0$  defined by (2.7):  $\Theta_{zx}^f(0) \approx 0.04$ , a property required for Bagnoldian-type bedload models (Pächtz & Durán 2018b). The fluid shear stress  $\sigma_{zx}^f$  is calculated from local quantities at the channel center as described in Chauchat (2018), assuming that the mixture viscosity obeys the closure measured by Boyer *et al.* (2011) for viscous suspensions. The dashed lines correspond to the bed surface elevations determined by Ni & Capart (2018).

transported grains ( $\sim M_*^2$ ) relative to that of grain-bed collisions ( $\sim M_*^1$ ). In fact, (3.1) expresses the balance between global energy production due to drag (left-hand side) and energy dissipation due to grain contacts (right-hand side). In order to apply it to non-spherical grains, it is important to generalize  $d$  in a manner that retains  $M_* \sim N$ . Since grains transported at elevations close to the bed surface, where most transport takes place, tend to align their largest projected area  $A_p^{\max}$  parallel to the bed due to torque (Jain *et al.* 2020; Zhang *et al.* 2025), implying  $M \sim N \rho_p V_p / A_p^{\max}$ , this requirement begets  $d \equiv \frac{3}{2} V_p / A_p^{\max}$ . From approximating grains as ellipsoids, we estimate  $V_p = \pi a_g b_g c_g / 6$  and  $A_p^{\max} = \pi a_g b_g / 4$ , leading to  $d = c_g$  (already used in figure 4A).

In steady, homogeneous sediment transport, the average vertical force acting on transported grains is dominated by gravity, buoyancy, and potentially fluid lift, since drag forces during the grains' upward motion tend to cancel those during their downward motion (Pächtz & Durán 2018a). When fluid lift is neglected, like in the simulations by Pächtz & Durán (2018b, 2020), this implies that the particle pressure at the bed surface  $-\sigma_{zz}^p(0)$  is approximately equal to the submerged particle weight  $M \tilde{g}_z$ . The bed friction coefficient  $\mu_b \equiv -\sigma_{zx}^p(0) / \sigma_{zz}^p(0)$  then links  $M \tilde{g}_z$  to the surface particle shear stress  $\sigma_{zx}^p(0)$ . When further separating  $\sigma_{zx}^p(0)$  into gravity and drag contributions and assuming that particle drag on the fluid reduces the surface fluid shear stress  $\sigma_{zx}^f(0)$  to a value that is just sufficient to sustain transport, one obtains after some rearrangements Bagnold's (Bagnold 1956) famous expression (Pächtz & Durán 2018b)

$$M_* = \frac{\Theta - \Theta_t}{\mu_b - \tan \alpha}, \quad (3.2)$$

which is a key ingredient of numerous bedload transport and windblown sand models in the

literature, including the one by Pahzt & Duran (2020). Historically, it has been assumed that  $\mu_b$  is equal to  $\mu_s$ , the tangent of the static angle of repose of the bulk bed material (Bagnold 1956). However, RANS-DEM simulations of turbulent bedload transport of spherical grains suggest that, although constant,  $\mu_b$  is actually substantially larger than  $\mu_s$  ( $\mu_b \approx 0.7$  versus  $\mu_s \approx 0.4$ ) (Pahzt & Duran 2018b). This observation can be understood as a bed surface strengthening effect (Clark *et al.* 2017; Allen & Kudrolli 2018; Cunez *et al.* 2022). Bedload transport increases the bed surface’s ability to resist shear stress, since temporarily mobilized grains can settle again in more stable bed surface pockets (Clark *et al.* 2017). Whenever this happens, the bed surface becomes stronger relative to the bulk, i.e.,  $r_b \equiv \mu_b/\mu_s$  increases. This process continuous until a state is reached at which the pockets that emerge at the places where grains are mobilized are equivalent to the most stable pockets that transported grains can reach (Clark *et al.* 2017). Then,  $r_b$  has acquired its equilibrium value and will no longer increase. In viscous bedload transport, where all pockets are reachable as a transported grain’s kinetic energy is typically much smaller than the potential energy wells of the bed surface,  $r_b \approx 3.4$  (Pahzt *et al.* 2021). However, in this study on turbulent bedload transport, where these two energy scales are of comparable size,  $r_b$  attains a smaller value as grains are too fast to probe the entire phase space of bed surface pockets (Clark *et al.* 2017). We use the value  $r_b = 1.8$  suggested by the simulations by Pahzt & Duran (2018b), where  $\mu_b \approx 0.7$  and  $\mu_s \approx 0.4$ , to calculate  $\mu_b = r_b\mu_s$  from the measured  $\mu_s$ .

In addition to using  $\mu_b = r_b\mu_s$ , we also generalize (3.2) to account for lift forces, defined as non-buoyancy fluid forces that act in the bed-normal direction. Neglecting particle-sidewall interactions in the particle momentum balance, a derivation analogous to that in Pahzt & Duran (2020) yields (Appendix C)

$$M_* = (\Theta - \Theta_t)/\mu^\dagger, \quad \text{with} \quad \mu^\dagger \equiv r_b\mu_s \left[ \frac{1 + \left(\frac{s \tan \alpha}{s-1} + \chi^*\right) \overline{f_L}/\overline{f_D}}{1 + r_b\mu_s \overline{f_L}/\overline{f_D}} \right] - \tan \alpha, \quad (3.3)$$

where  $\chi^* \equiv \chi/(\rho_p \bar{g}_z)$ ,  $f_D$  is the drag force per unit mass,  $f_L$  the lift force per unit mass divided by the fluid volume fraction  $1 - \phi$ , and the overbar,  $\bar{\cdot} \equiv \langle \phi \cdot \rangle_z / \langle \phi \rangle_z$ , denotes the  $\phi$ -weighted height average, that is, the average over all transported grains. The expression for  $\mu^\dagger$  takes into account that Reynolds stress gradients do not contribute to the buoyancy force (Maurin *et al.* 2018; Zhu *et al.* 2026), a recent finding that implies that there is no buoyancy force counteracting the gravitational and pressure gradient forces in the streamwise direction.

Equation (3.3) contains the single additional calibratable parameter  $\overline{f_L}/\overline{f_D}$  and reduces to (3.2) if fluid lift is neglected. In real-world scenarios, one may expect  $\overline{f_L}/\overline{f_D}$  to be of order unity, as suggested by measurements of drag and lift forces acting on surface roughness elements, including grains in bed surface pockets (Chepil 1958, 1961), and by DNS-DEM simulations of sheared mobile beds (Ji *et al.* 2013). We use  $\overline{f_L}/\overline{f_D} = 1.0$  because it optimizes the agreement between the final model and the entire data compilation.

### 3.1.2. Transport threshold

We reiterate that the prefactor  $2\sqrt{\Theta_t}/\kappa$  in (3.1) resulted from assuming that  $\Theta_t$  is the smallest Shields number that permits a quasi-continuous hopping-rebound motion (saltation) of a test grain along a stationary bed in a grain-motion-undisturbed logarithmic fluid velocity profile (Pahzt & Duran 2020). In such a scenario, lift forces acting on the moving test grain are typically much smaller than drag forces due to the formers’ rapid decrease with distance from the bed (Chepil 1961; Li *et al.* 2019). Then, it can be shown that, for conditions with  $s^{1/4}Ga \gtrsim 200$ ,  $\Theta_t$  in (3.1) obeys (Pahzt *et al.* 2021)

$$\Theta_t = c_t \left( r_b\mu_s - \frac{s}{s-1} \tan \alpha - \chi^* \right) / C_D, \quad (3.4)$$

where  $c_t$  is a dimensionless parameter and  $C_D$  an effective drag coefficient parametrizing streamwise drag force acting on grains. However, in spite of the similarity of (3.4) with scaling laws classically associated with the incipient motion of a grain resting in a bed surface pocket, we emphasize again that  $\Theta_t$  is not an incipient motion threshold but a so-called rebound threshold, as defined and discussed by Pahtz *et al.* (2020) and Pahtz *et al.* (2021). In particular, incipient motion thresholds have an additional dependence on  $h^*$  that is responsible for their often observed increase with bed slope  $\tan \alpha$  (Lamb *et al.* 2008), whereas  $\Theta_t$  in (3.4) always decreases with  $\tan \alpha$ .

The drag coefficient  $C_D$  in (3.4) is smaller than that for settling grains,  $C_{D\text{Settle}} = 4(s - 1)gd/(3v_s^2)$  (Deal *et al.* 2023), where  $v_s$  is the terminal grain settling velocity, due to the smaller projected grain area exposed to the flow. Assuming again that transported grains tend to align their largest projected area  $A_p^{\text{max}} = \pi a_g b_g/4$  parallel to the bed, the effective projected area  $A_p^{\text{eff}}$  in the streamwise direction is estimated as the geometric mean of the remaining two projected areas  $\pi a_g c_g/4$  and  $\pi b_g c_g/4$ :  $A_p^{\text{eff}} = \pi \sqrt{a_g b_g} c_g/4$ , implying  $A_p^{\text{eff}}/A_p^{\text{max}} = c_g/\sqrt{a_g b_g} \equiv S_f$ , which is the Corey shape factor. Hence, we obtain  $C_D = S_f C_{D\text{Settle}}$  or

$$C_D = 4S_f(s - 1)gd/(3v_s^2). \quad (3.5)$$

In the case of spherical grains ( $S_f = 1$ ), typical values for the quantities in (3.4) are  $\mu_s \approx 0.46$ ,  $C_D \approx 0.43$ , and  $\Theta_t \approx 0.05$  (Deal *et al.* 2023), implying  $c_t \approx 0.03$ . We use  $c_t = 0.032$  because it optimizes the agreement between the final model and the entire data compilation. On the other hand, when  $s^{1/4}Ga \lesssim 200$ , viscous-sublayer effects render the scaling of  $\Theta_t$  much more complicated (Pahtz *et al.* 2021). Therefore, we use (3.4) to determine  $\Theta_t$ , except for the few numerical conditions with  $s^{1/4}Ga < 200$  (BLRANSx in Table 1, where ‘x’ stands for an arbitrary character), for which we determine  $\Theta_t$  directly from the simulations, as described by Pahtz & Duran (2020). Note that the datasets J21DNS and KU17DNS in Table 1, which also satisfy  $s^{1/4}Ga < 200$ , are excluded from this discussion as they violate the precondition  $s^{1/2}Ga \gtrsim 80$  required for (3.1).

## 3.2. Extended data compilation

### 3.2.1. Experiments and grain-resolved CFD-DEM simulations

To evaluate our model, we require bedload flux datasets for shape-controlled grains, meaning they must provide the values of  $v_s$  and  $S_f$ , required to calculate  $C_D$  in (3.5), and the value of  $\mu_s$ , which affects  $Q_*$  both via the calculation of  $M_*$  in (3.3) and via the calculation of  $\Theta_t$  in (3.4). The datasets by Deal *et al.* (2023), denoted as D23EXPx in Table 1, and by Zhang *et al.* (2022, 2025), denoted as Z22LESx and Z25LESx in Table 1, satisfy this requirement. However, we excluded from Z25LESx simulation data based on the ‘‘artificial-shrinkage method’’ by Zhang *et al.* (2025), since this method has been falsified (Chen *et al.* 2026). Furthermore, in order to use the spherical-grain dataset NC18EXP by Ni & Capart (2018), who did not report  $\mu_s$ , we acquired the same spheres from the same company and measured  $\mu_s$  using the funnel method (Beakawi Al-Hashemi & Baghabra Al-Amoudi 2018) in the manner described by Deal *et al.* (2023): by slowly pouring them onto an elevated disk bounded by a  $2d_\sigma$ -high rim (Appendix D). Moreover, we scoured the literature and found two more usable experimental datasets for non-spherical grains: the bedload flux measurements for cylinders (R22EXPc) and lenses (R22EXPl) by Rebai *et al.* (2022). For both grain shapes,  $v_s$  (Matoušek & Zrostlık 2020) and the grain dimensions (required for  $S_f$ ) have been reported, while  $\mu_s$  was measured using the funnel method in a box filled with water, which was sufficiently large to rule out potential box-sidewall friction effects (private correspondence with the authors). We confirmed with DEM simulations that different procedures of conducting the funnel method

have only a small effect on  $\mu_s$  ( $< 5\%$ ) provided that a sufficiently large number of grains is used and that there is some means of preventing grains from rolling away (such as a rim or rough bed, see Appendix D). By contrast, most other experimental datasets reported in the literature, even well-controlled ones (Lajeunesse *et al.* 2010), do not report  $S_f$  and/or  $\mu_s$ .

For those datasets mentioned in the previous paragraph that were not already discussed in §2.4.1 on the spherical-grain data compilation, we use the values of  $h$  reported in the respective studies, as justified by  $h^* = h/d \gg 1$  (Table 1). For more details and the calculation of the bed shear stress uncertainty, see Appendix B.

### 3.2.2. Grain-unresolved CFD-DEM simulations

Since our bedload flux model generalizes (3.2), the transport load expression by Bagnold (1956), to (3.3), involving the additional parameter  $\overline{f_L/f_D} = 1.0$ , we test it also for conditions to which (3.2) applies (i.e.,  $\overline{f_L/f_D} = 0$ ). For this purpose, we add data from grain-unresolved CFD-DEM simulations to the compilation, both from existing studies (Pächt & Durán 2020; Maurin *et al.* 2018; Monthiller 2019) and from our own new simulations, all of which were conducted using either of the numerical models described by Durán *et al.* (2012), Maurin *et al.* (2015), or Xie *et al.* (2022) (Table 1, for details see Appendix E). They differ from grain-resolved simulations in the fact that they do not resolve the flow around single grains, and they therefore incorporate empirical relations for the buoyancy, drag, and lift forces acting on grains, the latter of which are typically neglected (also here, i.e.,  $\overline{f_L/f_D} = 0$ ). They also allow us to perform thought experiments in which  $C_D$  is treated as just another control parameter, since we can artificially modify  $C_D$  through changing the drag force parameters (Appendix E), see LESCD and BLRANSCD in Table 1. Another purpose of adding these data is to confront our bedload flux model with transport conditions across a much larger range of the control parameters  $\Theta$ ,  $\alpha$ , and  $h^*$  than that spanned by the experiments and grain-resolved simulations alone.

#### *Streamwise fluid momentum balance in BLRANSx*

The numerical model of Durán *et al.* (2012) behind the datasets BLRANSx considers a flow in an inner turbulent boundary layer of infinite height (no sidewalls). To be consistent with (2.5), we slightly modified the streamwise fluid momentum balance employed by Durán *et al.* (2012) to

$$d_z \sigma_{zx}^f = \rho_f \phi g \sin \alpha + \rho_p \phi f_x^{f \rightarrow p}, \quad \text{with} \quad \sigma_{zx}^f(\infty) = \tau_b, \quad (3.6)$$

before conducting simulations, where  $\rho_p \phi f_x^{f \rightarrow p}$  is the fluid-particle interaction force per unit volume of the mixture. In fact, integrating (3.6) from zero to infinity and combining the result with (C 5) and  $\sigma_{zx}(0) = \sigma_{zx}^f(0) + \sigma_{zx}^p(0)$  leads precisely to (2.5). Note that, for the numerical model of Durán *et al.* (2012), the Shields number  $\Theta \equiv \tau_b / (\rho_p \tilde{g}_z d)$  based on  $\tau_b$  in (3.6) is a prescribed fixed parameter.

#### *Determination of $\Theta$ for M18RANS, M19RANSx, and LESx*

Since the raw data required to determine the bed surface elevation, and thus  $h$  and  $\tau_b$ , are not available for the datasets M18RANS (Maurin *et al.* 2018) and M19RANSx (Monthiller 2019) in Table 1, based on the model of Maurin *et al.* (2015), we infer  $\Theta$  from their reported transport-driving Shields number  $\Theta_*$ , as explained in Appendix F.

### 3.3. Model validation

As a result of the wide range of control parameters and methods, especially grain shape parameters, the data of  $Q_*$  from the grain-unresolved simulations alone (figure 6A), and

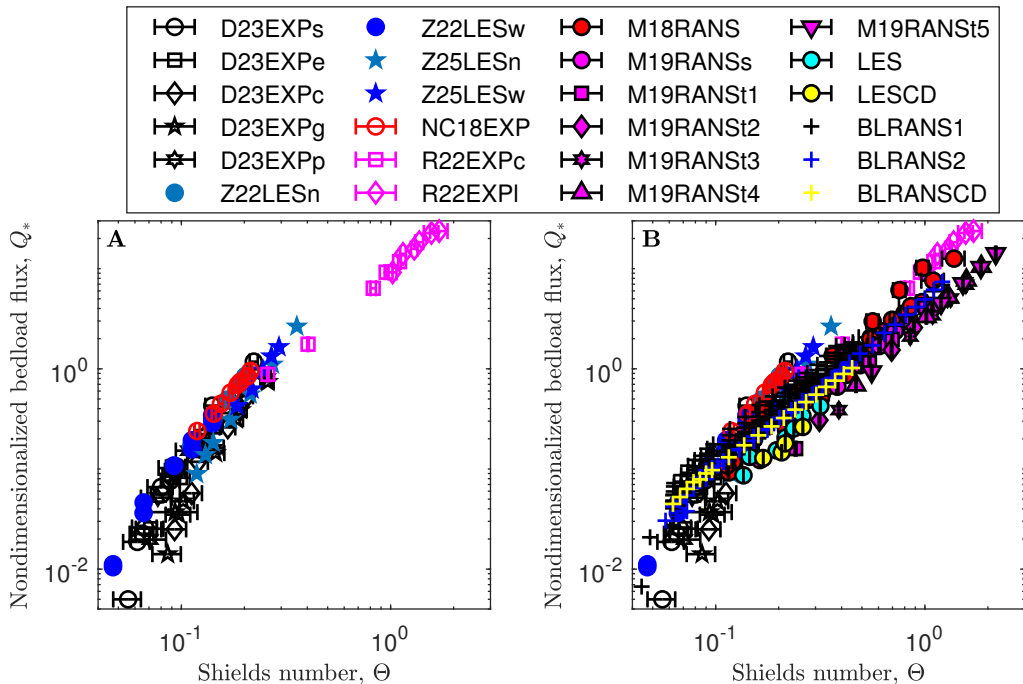


Figure 6: **Data compilation exhibits substantial scatter due to grain shape and other effects.** Nondimensionalized bedload flux  $Q_*$  versus Shields number  $\Theta$ , both rescaled using the generalized grain diameter definition  $d \equiv \frac{3}{2}V_p/A_p^{\max}$  (see text). Symbols in A correspond to data from channel-geometry-corrected experiments and grain-resolved CFD-DEM simulations (Table 1). Symbols in B also include grain-unresolved CFD-DEM simulations (Table 1). An error bar indicates the standard error and/or uncertainty range. In the absence of error bars, uncertainties are smaller than the symbol size.

in extension from the entire data compilation (figure 6B), can vary by almost an order of magnitude at a given channel-geometry-corrected Shields number  $\Theta$ . Nonetheless, the predictions from our bedload flux model deviate by less than a factor of 1.3 from almost all these data (figure 7). The only notable exception are the datasets Z25LESn and Z25LESw, which are based on the same grain shape. While the low- $\Theta$  simulations corresponding to these datasets are reproduced, their large- $\Theta$  simulations are substantially underpredicted (figures 7A and 7D).

As a side note, the agreement between our bedload flux model and most of the data compilation also lends support to the reliability of the grain-unresolved simulations, since, if they were governed by different physics, one would not expect them to be captured by the same physical analytical model.

## 4. Discussion

### 4.1. The role of fluid lift in bedload transport

Our rough-bedload flux model combines the global energy balance, (3.1) after Pätz & Durán (2020), linking the bedload flux to the transport load, with Bagnold's (Bagnold 1956) famous transport load expression, (3.3), generalized to account for a non-vanishing ratio  $f_L/f_D$  between the average lift and drag forces acting on transported grains. This is curious in so far as fluid lift is often assumed to be negligible in bulk bedload transport (Pätz & Durán

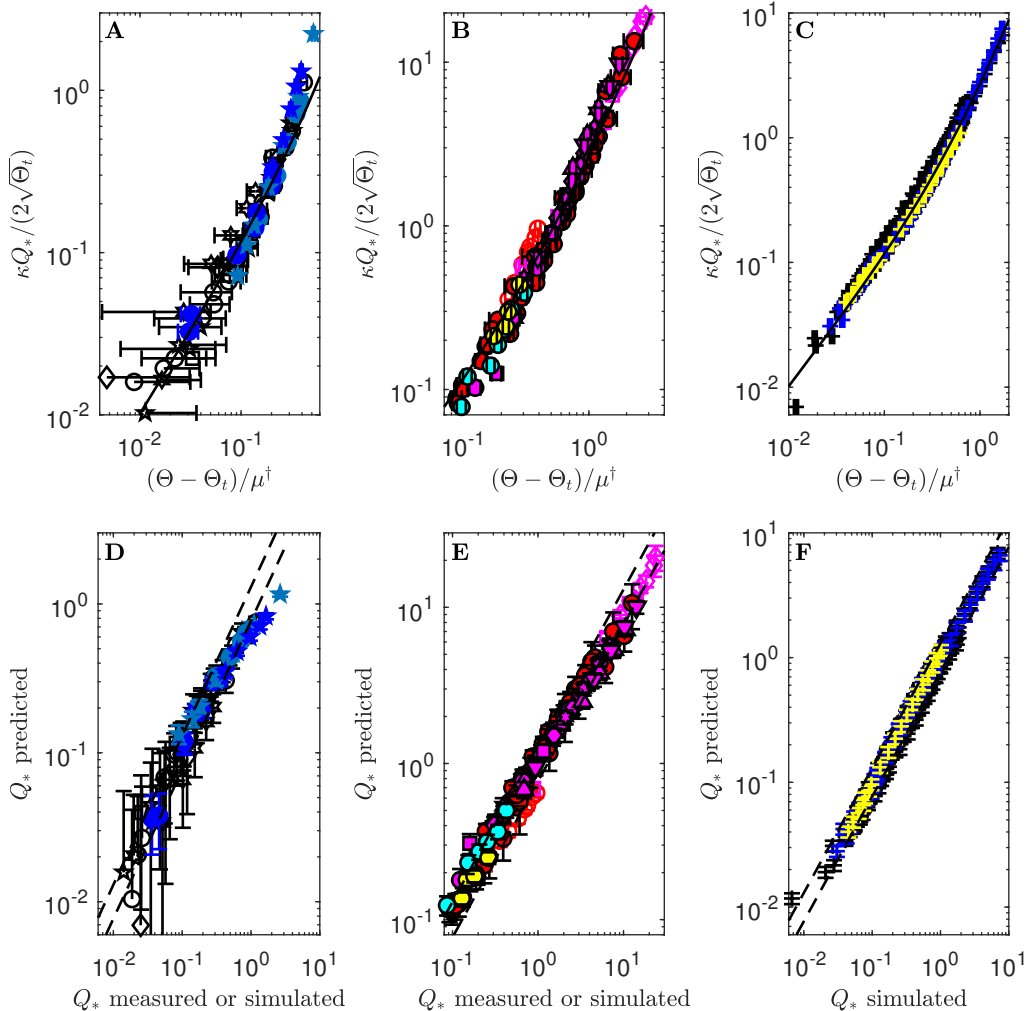


Figure 7: **Test of our rough-bedload flux model across grain shapes, bed slopes, flow strengths, and flow depths.** (A) Normalized bedload flux  $Y \equiv \kappa Q_* / (2\sqrt{\Theta_t})$  versus

$X \equiv (\Theta - \Theta_t) / \mu^\dagger$  and model prediction  $Y = X(1 + c_M X)$  (solid lines, from (3.1) and (3.3)). (D-F)  $Q_*$  predicted by (3.1) and (3.3) versus measured or simulated  $Q_*$ . Symbols correspond to channel-geometry-corrected data from a variety of methods (Table 1, see figure 6 for legend). An error bar indicates the standard error and/or uncertainty range. In

the absence of error bars, uncertainties are smaller than the symbol size. When  $s^{1/4} Ga \geq 200$ ,  $\Theta_t$  is calculated by (3.4). Otherwise (only BLRANSx),  $\Theta_t$  is determined directly from the simulations, as described in Pätz & Durán (2020). All grain-unresolved simulations neglect lift forces, implying  $\overline{f_L/f_D} = 0$ . Almost all data in D-F fall within a factor of 1.3 of the model prediction, delineated by the dashed lines.

2020; Pätz *et al.* 2021; Deal *et al.* 2023), mainly because once a grain is elevated above a stationary bed, the shear-induced lift force acting on it rapidly declines with elevation (Chepil 1961; Li *et al.* 2019) and may even become negative (Li *et al.* 2019; Shi & Rzehak 2019). In this regard, it is also interesting that  $\overline{f_L/f_D}$  has no bearing on the transport threshold  $\Theta_t$  in (3.4). (We confirmed that including  $\overline{f_L/f_D}$  in (3.4) in a fashion after Wiberg & Smith (1987) results in failure of the overall model.) The key difference between (3.3) and (3.4) is that the

former is modeling collective grain motion, whereas the latter is derived from the physical picture of a single test grain bouncing along an otherwise immobile bed. In DNS-DEM simulations, collective grain motion is highly associated with pressure-gradient-induced lift forces of a comparable magnitude to streamwise drag forces (Ji *et al.* 2013). By contrast, in DNS simulations of a fixed bed and a fixed particle elevated above it, such pressure-gradient-induced lift forces are much smaller than streamwise drag forces (Li *et al.* 2019). (Note that Li *et al.* (2019) called the pressure-gradient-induced lift forces “wall-normal drag forces”.) This suggest that collective grain motion might induce pressure fluctuations and thereby substantially enhance lift forces, though more studies are needed to test this hypothesis and, if confirmed, elucidate the underlying physical mechanism.

#### 4.2. Test of Deal *et al.*'s rough-bedload flux model with independent data

We are aware of only a single alternative bedload flux model attempting to account for grain shape: the one by Deal *et al.* (2023). These authors generalized  $d$  to the volume-equivalent sphere diameter  $d_o$ , as opposed to the shortest grain axis  $c_g \approx S_f^{2/3} d_o$  in our model, and used the modified Shields number  $\Theta^{D23} \equiv \tau_b / (\rho_p \tilde{g}_z d_o)$  and modified nondimensionalized bedload flux  $Q_*^{D23} \equiv Q / (\rho_p d_o \sqrt{(s-1)g d_o})$  to quantify the flow strength and transport rate, respectively. They proposed that bedload flux data corresponding to different grain shapes collapse onto a single curve  $Q_*^{D23} = f[(C^*/\mu^*)\Theta^{D23}]$ , where  $C^*$  is the sphere-normalized value of  $C_D d_o / c_g$  (Appendix G) and  $\mu^* \equiv (\mu_s - \tan \alpha) / (\mu_o - \tan \alpha)$ , with  $\mu_o = \tan 24^\circ$  the approximate value of  $\mu_s$  for spheres.

Deal *et al.* (2023) validated their model with their bedload flux measurements for several grain shapes, but not with other experimental data from independent sources. Here, we test their model with the independent datasets from our data compilation, sidewall-corrected with our derived universal method (figure 8). We remind the reader that, when applied to the datasets by Deal *et al.* (2023), this correction yields almost the same bed shear stress  $\tau_b$  as their own empirical correction (figure 4A), while unifying spherical-grain datasets across experimental facilities (figure 3D). So, any unfavorable outcome of this test is likely not attributable to the application of our method. To be as fair as possible, we focus on those independent datasets obtained from experiments and grain-resolved simulations (figures 8A–8D) and use the entire data compilation only as a secondary addition to our arguments (figures 8E and 8F). In addition, our main interest is not in the agreement between their model equation (solid lines in figures 8B and 8D) and the data, since this can be easily remedied through a change of the prefactor in that equation, but in the question of whether or not their Shields number correction reduces the scatter in the data.

It can be seen that the grain shape correction by Deal *et al.* (2023) (figures 8B and 8D) much increases the scatter in the independent data when compared with the situation without correction (figures 8A and 8C), both for intense and weak transport conditions. In particular, the chosen range 0.05–0.25 of the (un)corrected Shields number in figures 8C and 8D is equivalent to the range of their own experiments (Deal *et al.* 2023), and the maximum scatter in figure 8D by about a factor of 3 occurs well within this range, at  $(C^*/\mu^*)\Theta^{D23} \approx 0.14$ . It is mainly caused by the dataset R22EXPc in Table 1, for which  $C^*/\mu^* = 0.69$ , a more extreme value of  $C^*/\mu^*$  than in all their experiments ( $C^*/\mu^* = 0.84$ – $1.05$ ) (Deal *et al.* 2023).

We believe that this poor performance chiefly results from their incorporation of  $C^*$  in their grain shape correction of the Shields number. In fact, it was shown that models that express bedload flux as a function of the excess bed shear stress are inherently linked to the assumption by Bagnold (1956), later confirmed by Pätz & Durán (2018b), that the bed friction coefficient  $\mu_b$  is constant. (In the model of Deal *et al.* (2023),  $\mu_b = \mu_s$ , whereas  $\mu_b = r_b \mu_s$  in our model.) In equilibrium, this constant friction coefficient is equal to the

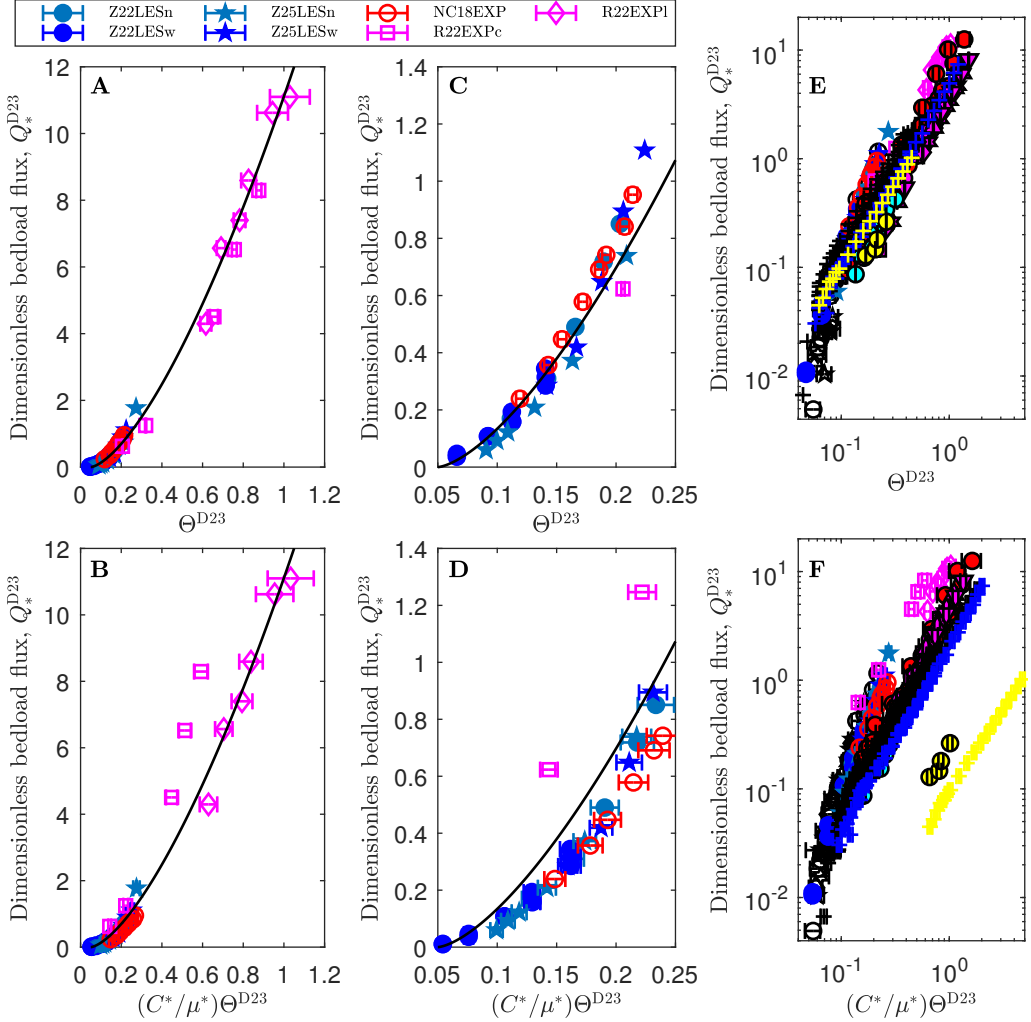


Figure 8: **Test of bedload flux model of Deal *et al.* (2023) with independent data.** Nondimensionalized bedload flux  $Q_*^{D23}$  versus shape-uncorrected Shields number  $\Theta^{D23}$  (A, C, E) and shape-corrected Shields number  $(C^*/\mu^*)\Theta^{D23}$  (B, D, F), based on the same definitions as Deal *et al.* (2023). Symbols in (A-D) correspond to data from channel-geometry-corrected experiments and grain-resolved simulations from independent studies. Symbols in (E, F) correspond to the entire channel-geometry-corrected data compilation, including D23EXPx (Deal *et al.* 2023) and data from grain-unresolved simulations (Table 1, see figure 6 for legend). An error bar indicates the standard error and/or uncertainty range. In the absence of error bars, uncertainties are smaller than the symbol size. The solid lines correspond to  $Q_*^{D23} = 12(\Theta^{D23} - 0.05)^{3/2}$  (A, C) and  $Q_*^{D23} = 12(\Theta^{D23} C^*/\mu^* - 0.05)^{3/2}$  (B, D). The latter is the prediction by Deal *et al.* (2023).

ratio between the average streamwise and bed-normal forces acting on transported grains, rendering the average drag force per unit mass  $\overline{f_D}$  insensitive to the details of the flow. In consequence, increments of  $C^*$  (or  $C_D$  in our model) tend to be compensated by decrements of the average fluid-particle velocity difference, keeping  $\overline{f_D}$  and therefore the effective transport-driving shear stress constant. Note that this reasoning is corroborated by the fact

that the yellow symbols in figures 8E and 8F, corresponding to conditions with artificially strongly elevated values of  $C^*$  or  $C_D$  (LESCD and BLRANSCD in Table 1), shift far away from the rest of the data after employing the grain shape correction by Deal *et al.* (2023). In contrast, they are captured by our bedload flux model (figure 7D) because it does not modify the Shields number  $\Theta$  by a drag-dependent correction.

## 5. Conclusions

We have derived a universal channel geometry correction method to determine the bed shear stress that collapses spherical-grain data of the nondimensionalized bedload flux  $Q_*$  as a function of the Shields number  $\Theta$  (figure 3), obtained from experiments and grain-resolved CFD-DEM simulations, across a wide range of geometries, including narrow-deep and wide-shallow open channel flows. It consists of a granular-physics-based method to determine the bed surface elevation and a sidewall correction derived from Kolmogórov's theory of turbulence. The latter incorporates a single parameter ( $c_{bw} \approx 2.23$  in (2.10)) that is exclusively related to approximately channel-geometry-independent scaling coefficients in that theory. We have applied the channel geometry correction method to a very diverse compilation of grain-shape-controlled datasets from experiments, grain-resolved, and grain-unresolved CFD-DEM simulations (Table 1). An existing bedload flux model, here generalized to account for grain shape effects, predicts almost all these data within a factor of 1.3 (figure 7). By contrast, the only, to our knowledge, existing alternative bedload model accounting for grain shape effects (Deal *et al.* 2023) clearly disagrees with the data compilation (figure 8). While our model agrees with the latter model in that the Corey shape factor  $S_f$ , static angle of repose  $\mu_s$ , and settling drag coefficient  $C_{D\text{Settle}}$  are the three relevant parameters for modeling grain shape, the effect of  $C_{D\text{Settle}}$  on  $Q_*$  is much weaker in our model, since it appears only via the transport threshold, and not also via a modification of  $\Theta$ . In §4.2, we have reasoned that a modification of  $\Theta$  via  $C_{D\text{Settle}}$  is unphysical, since it conflicts with the well-established result that the friction coefficient  $\mu_b$  at the interface between bed and transport layer is constant (Bagnold 1956; Pähtz & Durán 2018b). Another important difference between the two models is the meaning of the grain diameter  $d$  used to nondimensionalize physical quantities. Deal *et al.* (2023) assumed that  $d$  is equal to the volume-equivalent grain diameter  $d_o$ , whereas we reasoned that  $d$  should be the size  $c_g \approx S_f^{2/3} d_o$  of the shortest grain axis.

In view of the diversity of the data compilation in terms of sediment transport and channel flow conditions, and the methods it is based on, the degree by which our relatively simple model, with only three adjustable parameters, agrees with it is remarkable (figure 7). It suggests that, with the here employed sidewall correction and bed surface definition, and our physical model to predict the flux of rough bedload transport (applicable if  $s^{1/2}Ga \gtrsim 80$ , satisfied for most conditions in nature), bedload variability is largely diminished, at least for the idealized case considered here (steady flows over flat beds at short timescales). This is a prerequisite for discerning different sources of variability in the more complex situations typically encountered in nature.

**Acknowledgments.** The authors thank Yesheng Lu for helping finding grain-shape-controlled bedload transport datasets.

**Funding.** Z.H. acknowledges financial support from grant National Key R & D Program of China (2023YFC3008100). T.P. acknowledges financial support from grants National Natural Science Foundation of China (nos. 12350710176, 12272344). O.D. acknowledges financial support from Texas A&M Engineering Experiment Station.

**Declaration of interests.** The authors report no conflict of interest.

**Data availability statement.** The data required to reproduce figures 3, 4A, and 6-8, and 11, and a MATLAB

code to plot them are available online at <https://doi.org/10.5281/zenodo.19000875>. The measurements of  $\mu_s$  resulting from the experiment in figure 9 and simulations in figure 10 are reported in Table 1. The data plotted in figure 4B are from the tables of Guo (2015). The data plotted in figure 1 are from Ni & Capart (2018) and Deal *et al.* (2023) and can also be plotted using the MATLAB code. The data plotted in figures 2 and 5 are from the supplementary materials of Ni & Capart (2018). All data needed to evaluate the conclusions of the paper are present in the paper.

**Author contributions.** T.P. and Y.C. contributed equally.

## Appendix A. Einstein-Johnson's sidewall correction

The empirical sidewall correction by Einstein-Johnson calculates the friction factor ratio  $f_w/f_b$  in (2.8) as (Guo 2017)

$$\begin{aligned} f_w/f_b &= R_w/R_b, \quad \text{with} \quad R_b = (1 - 2R_w/b), \quad R_w = f^{-1}R[6\log_{10}[W(x)/x]]^{-2}, \\ f &= 8U^{-2}gR \sin \alpha, \quad x = [9\mathfrak{R}/(100f)]^{1/3}, \end{aligned} \tag{A 1}$$

where  $W(x)$  denotes the principal branch of the Lambert  $W$  function. These expressions constitute an analytical solution of the system of equations by Einstein (1942) and Johnson (1942), improving their iterative solution method as well as the graphical approximation by Vanoni & Brooks (1957).

## Appendix B. Estimation of bed shear stress and its uncertainty

### B.1. *NC18EXP*

For this highly-resolved dataset, the profiles of  $\dot{\gamma}\Sigma\phi$  exhibit several local maximums due to layering (figure 2). We choose the top-most local maximum at the bed surface elevation, defined in (2.7), because the profiles  $\Theta_{z,x}^f(z)$  exhibit a focal point there, with  $\Theta_{z,x}^f(0) \approx \Theta_t$  (figure 5), consistent with the theoretical expectation (Pächt & Durán 2018b). It occurs  $\Delta z = 31.75 \pm 0.5$  mm above the channel bottom for all flow conditions. The upper and lower bounds  $\Delta z = 32.25$  mm and  $\Delta z = 31.25$  mm then yield corresponding lower ( $h_{\min}$ ) and upper ( $h_{\max}$ ) bounds, respectively, of  $h$  for a given flow condition, with corresponding bed shear stress estimates  $\tilde{\tau}_b(h_{\max})$  and  $\tilde{\tau}_b(h_{\min})$ , respectively, obtained from (2.8) and (2.10). Hence, we estimate  $\tau_b$  and its uncertainty as

$$\tau_b = \frac{1}{2} [\tilde{\tau}_b(h_{\max}) + \tilde{\tau}_b(h_{\min})] \pm \frac{1}{2} [\tilde{\tau}_b(h_{\max}) - \tilde{\tau}_b(h_{\min})], \tag{B 1}$$

### B.2. *D23EXPx*, *R22EXPx*, *Z22LESx*, and *Z25LESx*

For these datasets, we use the reported values of  $h$  as its effect on  $\tau_b$  is very small because  $h$  was much larger than the bedload layer thickness (Deal *et al.* 2023; Zhang *et al.* 2022, 2025). Note that, for the numerical datasets *Z22LESx* and *Z25LESx*, we therefore conclude that the uncertainty of  $\tau_b$  is very small (smaller than the respective symbols in the plots). For the experimental datasets *D23EXPx*, the main source of uncertainty is the determination of the bed slope angle  $\alpha$ . We propagate its reported uncertainty to estimate the uncertainty of  $\tau_b$ . For the experimental datasets *R22EXPx*, the main source of uncertainty is the determination of  $h$ . We propagate its reported uncertainty to estimate the uncertainty of  $\tau_b$ .

### B.3. *J21DNS* and *KUI7DNS*

As we do not have access to the raw data of these datasets, and since  $h$  was much larger than the bedload thickness (Jain *et al.* 2021; Kidanemariam & Uhlmann 2017), we use the

reported values of  $h^*$  and  $\Theta$ , assuming that the uncertainty of  $\Theta$  is very small (smaller than the respective symbols in the plots).

#### B.4. M18RANS, M19RANSx, LESx

For these datasets, see Appendix F.

#### B.5. BLRANSx

For these datasets,  $h^* = \infty$  by construction and  $\Theta$  is a prescribed parameter (no uncertainty, see §3.2).

### Appendix C. Transport load expression

To derive simple expressions for the dimensionless transport load  $M_*$ , we neglect the contributions of particle-sidewall interactions in the streamwise and vertical particle momentum balances. Then, these balances read (Pächtz *et al.* 2026)

$$d_z \sigma_{zx}^P = -\rho_p \phi g \sin \alpha - \rho_p \phi f_x^{f \rightarrow P}, \quad (\text{C } 1)$$

$$d_z \sigma_{zz}^P = \rho_p \phi g \cos \alpha - \rho_p \phi f_z^{f \rightarrow P}, \quad (\text{C } 2)$$

where  $\rho_p \phi f^{f \rightarrow P}$  is the fluid-particle interaction force per unit volume of the mixture. In both balance equations, we decompose  $\rho_p \phi f^{f \rightarrow P}$  into buoyancy ( $\phi d_z \partial_i \sigma_{ix}$ ) and non-buoyancy contributions, where the latter are identified as the drag plus pressure gradient ( $\rho_p \phi f_D + \phi \chi$ ) and lift ( $\rho_p \phi \tilde{f}_L$ ) forces per unit volume of the mixture for the streamwise and vertical directions, respectively:

$$f_x^{f \rightarrow P} = f_D + \chi / \rho_p + d_z (\sigma_{zx} - \sigma_{\text{Re}zx}) / \rho_p \simeq f_D + \chi / \rho_p, \quad (\text{C } 3)$$

$$f_z^{f \rightarrow P} = \tilde{f}_L + d_z (\sigma_{zz} - \sigma_{\text{Re}zz}) / \rho_p \simeq \tilde{f}_L + d_z \sigma_{zz} / \rho_p = \frac{\tilde{f}_L}{1 - \phi} + s^{-1} g \cos \alpha, \quad (\text{C } 4)$$

The buoyancy contribution in (C3) has been neglected, since the effective fluid shear stress  $\sigma_{zx}$  is dominated by the Reynolds stress  $\sigma_{\text{Re}zx}$ , gradients of which do not contribute to buoyancy (Maurin *et al.* 2018; Zhu *et al.* 2026). By contrast, the effective fluid pressure  $\sigma_{zz}$  dominates the Reynolds pressure  $\sigma_{\text{Re}zz}$ , leading to a standard buoyancy expression (Durán *et al.* 2012, e.g.,). Using (C3) and (C4), integration of (C1) and (C2), respectively, yields

$$\sigma_{zx}^P(0) = M \left( g \sin \alpha + \chi / \rho_p + \overline{f_D} \right), \quad (\text{C } 5)$$

$$\sigma_{zz}^P(0) = -M \left( \tilde{g}_z - \overline{f_L} \right), \quad (\text{C } 6)$$

where  $f_L \equiv \tilde{f}_L / (1 - \phi)$ . It follows that the bed friction coefficient,  $\mu_b \equiv -\sigma_{zx}^P(0) / \sigma_{zz}^P(0)$ , constrains the average forces acting on transported grains:

$$\mu_b = \frac{g \sin \alpha + \chi / \rho_p + \overline{f_D}}{\tilde{g}_z - \overline{f_L}}. \quad (\text{C } 7)$$

This equation can be transformed into

$$\overline{f_D} = \frac{\mu_b \tilde{g}_z - g \sin \alpha - \chi / \rho_p}{1 + \mu_b \overline{f_L} / \overline{f_D}}. \quad (\text{C } 8)$$

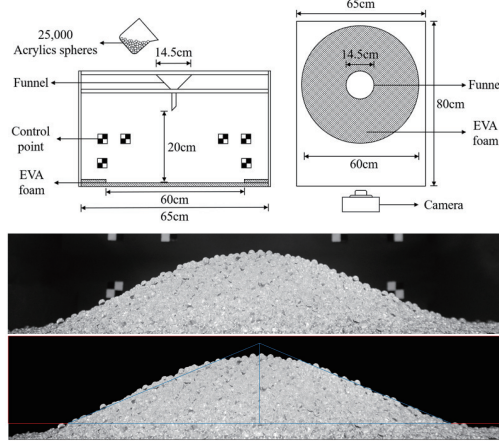


Figure 9: **Measurements of  $\mu_s$  for the dataset NC18EXP (Table 1)**. We slowly poured 25,000 grains onto an elevated disk bounded by a  $2d$ -high rim. The angle of repose of the resulting heap is then determined as the base angle of the isosceles triangle that has the same area as the projected heap, averaged over two side-view images separated by a rotation of  $90^\circ$  (Elekesa & Parteli 2021).

Finally, combining (C5) and (C8) with (2.5) and  $\sigma_{zx} = \sigma_{zx}^f + \sigma_{zx}^p$ , nondimensionalizing, and employing  $\Theta - \Theta_{zx}^f(0) \equiv (\tau_b - \sigma_{zx}^f(0))/(\rho_p \tilde{g}_z d) = \Theta - \Theta_t$  (Pächtz & Durán 2018b) leads to (3.3).

## Appendix D. Determinations of angle of repose and its uncertainty

We acquired the same spheres as those used in Ni & Capart (2018) (NC18EXP in Table 1) from the same company (Chiao Dar Acry & Advertisement Co., Ltd., <http://www.bridgeacry.com.tw>) and measured  $\mu_s$  using the funnel method (Beakawi Al-Hashemi & Baghabra Al-Amoudi 2018) in the manner described in Deal *et al.* (2023) (figure 9). Furthermore, we confirmed with DEM simulations that different measurement methods have only a small effect on  $\mu_s$  provided that a sufficiently large number of grains is used and that there is some means of preventing grains from rolling away (such as a rim or a rough bed, see figure 10). Based on these simulations, we assign an uncertainty of 5% to all  $\mu_s$ -measurements, including those from different studies and methods.

## Appendix E. Grain-unresolved simulation details

### E.1. Contact parameters and $\mu_s$ in grain-unresolved CFD-DEM simulations

The normal restitution coefficient  $e_n$ , tangential contact friction coefficient  $\mu_c$ , and tangent of the static angle of repose,  $\mu_s$  (determined as described in figure 10), are  $(e_n, \mu_c, \mu_s) = (0.5, 0.4, 0.40)$  for the model of Maurin *et al.* (2015) and data of Maurin *et al.* (2018),  $(e_n, \mu_c, \mu_s) = (0.5, 0.5, 0.49\text{--}0.72)$  for the model of Maurin *et al.* (2015) and data of Monthiller (2019),  $(e_n, \mu_c, \mu_s) = (0.9, 0.5, 0.38)$  for the model of Durán *et al.* (2012), and  $(e_n, \mu_c, \mu_s) = (0.3, 0.5, 0.49)$  for the model of Xie *et al.* (2022).

### E.2. Drag coefficient

The numerical CFD-DEM models that do not resolve the sub-grain scale rely on semiempirical relations for fluid-particle interactions. They consider buoyancy and drag forces on

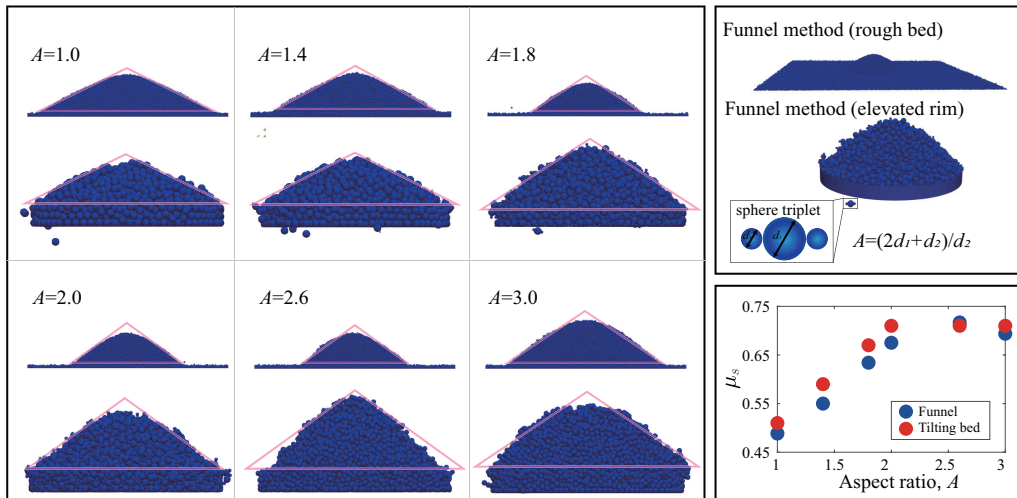


Figure 10: **Numerical determination of the static angle of repose.** We compare three different methods of measuring the tangent of the static angle of repose,  $\mu_s$ , for the composite grains (spheres and sphere triplets) used in the grain-unresolved DEM-CFD simulations: slowly pouring a sufficient number of grains onto a rough bed consisting of spheres of the same volume-equivalent sphere diameter  $d_o$  (funnel method 1), onto an elevated disk of diameter  $24d_o$  bounded by a  $2d_o$ -high rim (funnel method 2, exactly as described in Deal *et al.* (2023)), and tilting the granular bed until the granular bulk moves (tilting method). The most reliable and reproducible results are yielded by funnel method 1, where the angle of repose is determined as the base angle of the isosceles triangle that has the same area as the projected heap, averaged over two side-view images separated by a rotation of  $90^\circ$  (Elekes & Parteli 2021). For funnel method 2, the heaps exhibit too irregular shapes when the aspect ratio  $A$  becomes too large, making a clear determination of the angle of repose difficult. However, for  $A \lesssim 2$ , it yields values very close to funnel method 1. The tilting method also yields similar results as funnel method 1, though it is sometimes difficult to distinguish between bulk and isolated-grain motion. We therefore decided to use funnel method 1 as the standard procedure to determine  $\mu_s$  in the grain-unresolved DEM-CFD simulations.

spheres or composite grains consisting of non-overlapping component spheres, but neglect lift forces. Following Sun *et al.* (2017), the drag force is modeled as the total force on all component spheres:

$$\mathbf{F}_D = \sum_i \frac{1}{8} \rho_f \pi d_i^2 \left[ \left( \frac{\mathfrak{R}_c \nu}{d_i \epsilon^{p_1}} \right)^{1/m} + \left( \frac{C_D^\infty |\mathbf{u}_r|}{\epsilon^{p_2}} \right)^{1/m} \right]^m \mathbf{u}_r, \quad (\text{E } 1)$$

where  $d_i$  is the diameter of the  $i$ -th component sphere,  $\mathbf{u}_r$  the fluid-particle velocity difference, and  $\mathfrak{R}_c$ ,  $C_D^\infty$ ,  $m$ ,  $p_1$ , and  $p_2$  are empirical parameters. They are  $(\mathfrak{R}_c, C_D^\infty, m, p_1, p_2) = (24.4, 0.4, 1, 3.1, 3.1)$  in Maurin *et al.* (2015),  $(\mathfrak{R}_c, C_D^\infty, m, p_1, p_2) = (24, 0.5, 2, 0, 0)$  in Durán *et al.* (2012) (nominal),  $(\mathfrak{R}_c, C_D^\infty, m, p_1, p_2) = (96, 2, 2, 0, 0)$  in Durán *et al.* (2012) (enhanced drag),  $(\mathfrak{R}_c, C_D^\infty, m, p_1, p_2) = (23.04, 0.3969, 2, p, p - 1)$  in Xie *et al.* (2022) (nominal), and  $(\mathfrak{R}_c, C_D^\infty, m, p_1, p_2) = (69.12, 1.1907, 2, p, p - 1)$  in Xie *et al.* (2022) (enhanced drag), with  $p = 3.7 - 0.65 \exp[-(1.5 - \log_{10}(\epsilon |\mathbf{u}_r| d_i / \nu))^2 / 2]$ . Dividing (E 1) by the grain weight  $\frac{\pi}{6} \sum_i d_i^3$  leads to an expression for the ratio between the drag acceleration  $\mathbf{a}_D$  and submerged gravitational acceleration  $\tilde{g} \equiv (1 - 1/s)g$  in terms of nondimensionalized

quantities:

$$\frac{\mathbf{a}_D}{\tilde{g}} = \frac{3}{4} \left[ \left( \frac{\mathfrak{K}_c}{\overline{Ga} \epsilon^{p_1}} \right)^{1/m} + \left( \frac{C_D^\infty |\tilde{\mathbf{u}}_r|}{\epsilon^{p_2}} \right)^{1/m} \right]^m \tilde{\mathbf{u}}_r, \quad (\text{E } 2)$$

where  $\tilde{\mathbf{u}}_r \equiv \mathbf{u}_r / \sqrt{s \tilde{g} d}$ , with  $d \equiv \frac{3}{2} V_p / A_p^{\max} = \sum_i d_i^3 / \sum_i d_i^2$ , is the nondimensionalized fluid-particle velocity difference and

$$\overline{Ga} \equiv \frac{\sqrt{(\sum_i d_i^2) (\sum_i d_i^3)}}{\sum_i d_i} \sqrt{s \tilde{g} / \nu} \quad (\text{E } 3)$$

a quantity similar to the Galileo number. From (E 2), one obtains the nondimensionalized settling velocity  $\tilde{v}_s$  of a single composite grain in quiescent fluid ( $\epsilon = 1$ ) as (Pächtz *et al.* 2021)

$$\tilde{v}_s = \left[ \sqrt{\frac{1}{4} \left[ \sqrt{\left( \frac{\mathfrak{K}_c}{C_D^\infty \overline{Ga}} \right)^2 + m \sqrt{\frac{4}{3 C_D^\infty}}} - \frac{1}{2} \sqrt{\frac{\mathfrak{K}_c}{C_D^\infty \overline{Ga}}} \right]^m} \right] \quad (\text{E } 4)$$

and subsequently the drag coefficient as

$$C_D = \frac{4(s-1)gd}{3v_s^2} = \frac{4}{3\tilde{v}_s^2}. \quad (\text{E } 5)$$

Here we used that a composite grain is treated as if the projected area of all its component spheres is always, regardless of its orientation relative to the flow, fully exposed to the flow, which follows from (E 1). That is, the total projected area seen by the flow,  $A_p = \frac{\pi}{4} \sum_i d_i^2$ , is constant, and therefore  $A_p^{\text{eff}} = A_p^{\max}$  and  $C_D = C_{D\text{Settle}}$ .

## Appendix F. Determination of $\Theta$ for M18RANS, M19RANSx, and LESx

For the datasets M18RANS (Maurin *et al.* 2018) and M19RANSx (Monthiller 2019) in Table 1, based on the model of Maurin *et al.* (2015), only the transport-driving Shields number  $\Theta_*$  is reported. Maurin *et al.* (2015) defined  $\Theta_* \equiv \tau_{\text{cl}} / (\rho_p \tilde{g}_z d)$  as the Shields number based on the clear-water fluid shear stress  $\tau_{\text{cl}}$  on the top of the bedload layer:

$$\tau_{\text{cl}} \equiv \max \sigma_{zx}^f(z). \quad (\text{F } 1)$$

Using  $\tau_b \propto h$  for their sidewall-free channels,  $\tau_{\text{cl}}$  therefore defines an effective clear-flow depth as

$$h_{\text{cl}} \equiv h \tau_{\text{cl}} / \tau_b \quad (\text{F } 2)$$

and subsequently an effective bedload layer thickness above the bed surface as

$$h_p \equiv h - h_{\text{cl}}. \quad (\text{F } 3)$$

The latter is linked to the transport load  $M$  via

$$M = \rho_p h_p \underline{\phi}, \quad (\text{F } 4)$$

with  $\underline{\phi} \equiv \frac{1}{h_p} \int_0^h \phi dz \approx \frac{1}{h_p} \int_0^{h_p} \phi dz$  the approximate average of the particle volume fraction  $\phi$  over the bedload layer thickness. Combining the above relations and nondimensionalizing

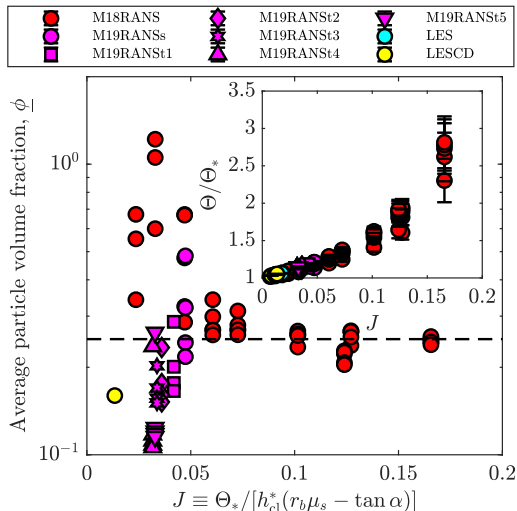


Figure 11: **Determination of transport-layer-averaged particle volume fraction  $\underline{\phi}$ .**  $\underline{\phi}$ , estimated from the  $Q_*$ -data as described in the text, versus  $J$ . Symbols correspond to grain-unresolved CFD-DEM simulations (Table 1). The dashed line indicates the value  $\underline{\phi} = 0.25$  exhibited for large  $J$ , where the ratio  $\Theta/\Theta_*$  deviates from unity the most. Inset: Estimate of  $\Theta/\Theta_*$  resulting from  $\underline{\phi} = 0.25$ , where the error bars correspond to the propagated uncertainty of  $\mu_s$ , required for predicting  $M_*$  and therefore  $\Theta$ , as described in the text.

the result yields

$$\Theta = \Theta_* \left( 1 + \frac{M_*}{\underline{\phi} h_{cl}^*} \right), \quad (\text{F5})$$

where  $h_{cl}^* \equiv h_{cl}/d$  is the dimensionless clear-flow depth.

To determine the parameter  $\underline{\phi}$  in (F5), we combine (F5) with (3.2), valid for the grain-unresolved simulations due to  $\overline{f_L}/\overline{f_D} = 0$ , yielding

$$\underline{\phi} = J \left( 1 - \frac{\Theta_* - \Theta_t}{(r_b \mu_s - \tan \alpha) M_*} \right)^{-1}, \quad (\text{F6})$$

with  $J \equiv \Theta_* / [h_{cl}^* (r_b \mu_s - \tan \alpha)]$ . The unknown values of  $M_*$  in (F6) can be estimated from the simulation data of  $Q_*$  via (3.1), using the predicted values of  $\Theta_t$  from (3.4). Figure 11 shows the resulting *estimates* of  $\underline{\phi}$  as a function of  $J$  for the grain-unresolved datasets M18RANS, M19RANS $x$ , LES, and LESCD. Note that the estimates for  $J \lesssim 0.05$  cannot be trusted, since they are very sensitive to even slight variations in the simulation data of  $\Theta_*$ ,  $h_{cl}^*$ , and especially  $Q_*$ , explaining the large scatter and the occasionally unphysically large values of  $\underline{\phi}$  for low  $J$ . However, this is not a serious issue, since for weak transport conditions,  $\Theta_*$  is close to  $\Theta$  no matter the precise value of  $\underline{\phi}$  as  $M_*$  in (F5) becomes small. By contrast, for  $J \gtrsim 0.05$ , the estimations of  $\underline{\phi}$  from the simulation data scatter relatively little between only about 0.2 and 0.3 (figure 11). In particular, for the most intense conditions,  $\underline{\phi} \simeq 0.25$ , which is a reasonable value as it is about half of  $\phi(0)$  for intense transport conditions (Pätz & Durán 2018b). We therefore fix  $\underline{\phi} = 0.25$  in (F5) as a simple means to relate  $\Theta$  to  $\Theta_*$  for arbitrary conditions through (F5). The ratio  $\Theta/\Theta_*$  resulting from this choice is shown in the inset of figure 11.

Although we have used the  $M_*$ -values estimated from the  $Q_*$ -data via (3.1) to obtain  $\underline{\phi} = 0.25$ , we do not do so when estimating  $\Theta$  from (F5), in order to avoid an implicit dependence of  $\Theta$  on  $Q_*$ . Instead, we obtain  $\Theta$  from the values of  $M_*$  predicted by (3.3). The uncertainty of  $\Theta$  then corresponds to the propagated uncertainty of  $\mu_s$  in the calculation of  $\Theta$  via (3.3) and (F5).

## Appendix G. Sphere-normalized drag coefficient after Deal *et al.* (2023)

Deal *et al.* (2023) defined the sphere-normalized drag coefficient  $C^*$  as

$$C^* \equiv S_f v_o^2 / v_s^2, \quad (\text{G } 1)$$

where  $v_o$  is the theoretical value of the settling velocity of spheres, given via (Dietrich 1982; Deal *et al.* 2023)

$$v_{o*} = -3.81564 + 1.94593D_* - 0.09016D_*^2 - 0.00855D_*^3 + 0.00075D_*^4, \quad (\text{G } 2)$$

with  $v_{o*} \equiv \log_{10} v_o^3 / [(s-1)g\nu]$ ,  $D_* \equiv \log_{10}(s-1)gd_o^3/\nu^2$ . Since these expressions are based on the volume-equivalent sphere diameter  $d_o$ , as opposed to the shortest grain axis  $c_g$  in our model,  $C^*$  is linked to the drag coefficient  $C_D$  in (3.5) through  $C^* = C_D d_o / (C_o c_g)$ , where  $C_o \equiv 4(s-1)gd_o/(3v_o^2)$ .

## REFERENCES

- AGUDO, J. R., ILLIGMANN, C., LUZI, G., LAUKART, A., DELGADO, A. & WIERSCHEM, A. 2017 Shear-induced incipient motion of a single sphere on uniform substrates at low particle Reynolds numbers. *Journal of Fluid Mechanics* **825**, 284–314.
- ALLEN, B. & KUDROLLI, A. 2018 Granular bed consolidation, creep, and armoring under subcritical fluid flow. *Physical Review Fluids* **3** (7), 074305.
- ANCEY, C. 2020 Bedload transport: a walk between randomness and determinism. Part 1. The state of the art. *Journal of Hydraulic Research* **58** (1), 1–17.
- ANCEY, C. & RECKING, A. 2023 Scaling behavior of bedload transport: what if bagnold was right? *Earth-Science Reviews* **246**, 104571.
- ANTONIA, R.A. & PEARSON, B.R. 2000 Reynolds number dependence of velocity structure functions in a turbulent pipe flow. *Flow, Turbulence and Combustion* **64** (2), 95–117.
- ARMANINI, A. & CAVEDON, V. 2019 Bed-load through emergent vegetation. *Advances in Water Resources* **129**, 250–259.
- AUEL, C., ALBAYRAK, I. & BOES, R. M. 2014 Turbulence characteristics in supercritical open channel flows: Effects of froude number and aspect ratio. *Journal of Hydraulic Engineering* **140** (4), 04014004.
- AUSSILLOUS, P., CHAUCHAT, J., PAILHA, M., MÉDALE, M. & GUZZELLI, É 2013 Investigation of the mobile granular layer in bedload transport by laminar shearing flows. *Journal of Fluid Mechanics* **736**, 594–615.
- BAGNOLD, R. A. 1956 The flow of cohesionless grains in fluid. *Philosophical Transactions of the Royal Society London A* **249** (964), 235–297.
- BAKER, VICTOR R., HAMILTON, CHRISTOPHER W., BURR, DEVON M., GULICK, VIRGINIA C., KOMATSU, GORO, LUO, WEI, RICE, JAMES W. & RODRIGUEZ, J.A.P. 2015 Fluvial geomorphology on Earth-like planetary surfaces: A review. *Geomorphology* **245**, 149–182.
- BEAKAWI AL-HASHEMI, H. M. & BAGHABRA AL-AMOUDI, O. S. 2018 A review on the angle of repose of granular materials. *Powder Technology* **330**, 397–417.
- BOYER, F., GUZZELLI, É & POULIQUEN, O. 2011 Unifying suspension and granular rheology. *Physical Review Letters* **107** (18), 188301.
- CAPART, H. & FRACCAROLLO, L. 2011 Transport layer structure in intense bed-load. *Geophysical Research Letters* **38** (20), L20402.
- CARRILLO, V., PETRIE, J., TIMBE, L., PACHECO, E., ASTUDILLO, W., PADILLA, C. & CISNEROS, F. 2022 Validation of an experimental procedure to determine bedload transport rates in steep channels with coarse sediment. *Water* **13**, 672.

- CHARRU, F., ANDREOTTI, B. & CLAUDIN, P. 2013 Sand ripples and dunes. *Annual Review of Fluid Mechanics* **45**, 469–493.
- CHARRU, F., MOUILLERON, H. & EIFF, O. 2004 Erosion and deposition of particles on a bed sheared by a viscous flow. *Journal of Fluid Mechanics* **519**, 55–80.
- CHAUCHAT, J. 2018 A comprehensive two-phase flow model for unidirectional sheet-flows. *Journal of Hydraulic Research* **56** (1), 15–28.
- CHEN, Y., DURÁN, O. & PÄHTZ, T. 2026 On the testing of grain shape corrections to bedload transport equations with grain-resolved numerical simulations. *Earth Surface Dynamics* **14**, 75–83.
- CHEPIL, W. S. 1958 The use of evenly spaced hemispheres to evaluate aerodynamic forces on a soil surface. *Transcripts of the American Geophysical Union* **39**, 397–403.
- CHEPIL, W. S. 1961 The use of spheres to measure lift and drag on wind-eroded soil grains. *Soil Science Society of America Journal* **25** (5), 343–345.
- CLARK, A. H., SHATTUCK, M. D., OUELLETTE, N. T. & O'HERN, C. S. 2017 Role of grain dynamics in determining the onset of sediment transport. *Physical Review Fluids* **2** (3), 034305.
- CÚÑEZ, FERNANDO D., FRANKLIN, E. M., HOUSSAIS, M., ARRATIA, P. & JEROLMACK, D. J. 2022 Strain hardening by sediment transport. *Physics Review Research* **4** (2), L022055.
- DEAL, E., VENDITTI, J. G., BENAVIDES, S. J., BRADLEY, R., ZHANG, Q., KAMRIN, K. & PERRON, J. T. 2023 Grain shape effects in bed load sediment transport. *Nature* **613**, 298–302.
- DHONT, B. & ANCEY, C. 2018 Are bedload transport pulses in gravel bed rivers created by bar migration or sediment waves? *Geophysical Research Letters* **45** (11), 5501–5508.
- DIETRICH, W. E. 1982 Settling velocity of natural particles. *Water Resources Research* **18** (6), 1615–1626.
- DURÁN, O., ANDREOTTI, B. & CLAUDIN, P. 2012 Numerical simulation of turbulent sediment transport, from bed load to saltation. *Physics of Fluids* **24** (10), 103306.
- DURÁN VINENT, O., ANDREOTTI, B., CLAUDIN, P. & WINTER, C. 2019 A unified model of ripples and dunes in water and planetary environments. *Nature Geoscience* **12**, 345–350.
- EINSTEIN, H. A. 1942 Formulas for the transportation of bedload. *Transactions of ASCE* **107**, 561–597.
- ELEKESA, F. & PARTELI, E. J. R. 2021 An expression for the angle of repose of dry cohesive granular materials on earth and in planetary environments. *Proceedings of the National Academy of Sciences of the United States of America* **118** (38), e2107965118.
- FREY, PHILIPPE 2014 Particle velocity and concentration profiles in bedload experiments on a steep slope. *Earth Surface Processes and Landforms* **39** (5), 646–655.
- FREY, P., DUFRESNE, M., BÖHM, T., JODEAU, M. & ANCEY, C. 2006 Experimental study of bed load on steep slopes. In *River Flow 2006*, pp. 887–893. London, UK: Taylor & Francis Group.
- GIOIA, G. & BOMBARDELLI, F. A. 2002 Scaling and similarity in rough channel flows. *Physical Review Letters* **88** (1), 014501.
- GIOIA, G. & PINAKI CHAKRABORTY 2006 Turbulent friction in rough pipes and the energy spectrum of the phenomenological theory. *Physical Review Letters* **96** (4), 044502.
- GUO, J. 2015 Sidewall and non-uniformity corrections for flume experiments. *Journal of Hydraulic Research* **53** (2), 218–229.
- GUO, J. 2017 Exact procedure for Einstein-Johnson's sidewall correction in open channel flow. *Journal of Hydraulic Engineering* **143** (4), 06016027.
- HOUSSAIS, M., ORTIZ, C. P., DURIAN, D. J. & JEROLMACK, D. J. 2015 Onset of sediment transport is a continuous transition driven by fluid shear and granular creep. *Nature Communications* **6**, 6527.
- JAIN, R., TSCHISGALE, S. & FRÖHLICH, J. 2020 Effect of particle shape on bedload sediment transport in case of small particle loading. *Meccanica* **55**, 299–315.
- JAIN, R., TSCHISGALE, S. & FRÖHLICH, J. 2021 Impact of shape: Dns of sediment transport with non-spherical particles. *Journal of Fluid Mechanics* **916**, A38.
- JI, C., MUNJIZA, A., AVITAL, E., MA, J. & WILLIAMS, J. J. R. 2013 Direct numerical simulation of sediment entrainment in turbulent channel flow. *Physics of Fluids* **25** (5), 056601.
- JOHNSON, J. W. 1942 The importance of considering sidewall friction in bed-load investigations. *Civil Engineering* **12**, 329–332.
- KIDANEMARIAM, A. G. 2016 The formation of patterns in subaqueous sediment. PhD thesis, Karlsruhe Institute of Technology, Karlsruhe, Germany.
- KIDANEMARIAM, A. G. & UHLMANN, M. 2017 Formation of sediment patterns in channel flow: minimal unstable systems and their temporal evolution. *Journal of Fluid Mechanics* **818**, 716–743.
- LAJEUNESSE, E., MALVERTI, L. & CHARRU, F. 2010 Bed load transport in turbulent flow at the grain scale: Experiments and modeling. *Journal of Geophysical Research: Earth Surface* **115** (F4), F04001.

- LAMB, M. P., DIETRICH, W. E. & VENDITTI, J. G. 2008 Is the critical Shields stress for incipient sediment motion dependent on channel-bed slope? *Journal of Geophysical Research* **113**, F02008.
- LI, X., BALACHANDAR, S., LEE, H. & BAI, B. 2019 Fully resolved simulations of a stationary finite-sized particle in wall turbulence over a rough bed. *Physical Review Fluids* **4** (9), 094302.
- MATOUŠEK, V. & ZROSTLÍK, Š 2020 Collisional transport model for intense bed load. *Journal of Hydrology and Hydromechanics* **68** (1), 60–69.
- MAURIN, R., CHAUCHAT, J., CHAREYRE, B. & FREY, P. 2015 A minimal coupled fluid-discrete element model for bedload transport. *Physics of Fluids* **27** (11), 113302.
- MAURIN, R., CHAUCHAT, J. & FREY, P. 2018 Revisiting slope influence in turbulent bedload transport: consequences for vertical flow structure and transport rate scaling. *Journal of Fluid Mechanics* **839**, 135–156.
- MEYER-PETER, E. & MÜLLER, R. 1948 Formulas for bedload transport. In *Proceedings of the 2nd Meeting of the International Association for Hydraulic Structures Research*, pp. 39–64. IAHR, Stockholm.
- MONTHILLER, R. 2019 Particle shape influence on turbulent bedload transport. Master's thesis, ENSEEIHT, University of Toulouse, Toulouse, France.
- NI, W. J. & CAPART, H. 2018 Stresses and drag in turbulent bed load from refractive index-matched experiments. *Geophysical Research Letters* **45**, 7000–7009.
- NIKITIN, N. V., NICLOUD, F., WASISTHO, B., SQUIRES, K. D. & SPALART, P. R. 2000 An approach to wall modeling in large-eddy simulations. *Physics of Fluids* **12** (7), 1629.
- NIKURADSE, J. 1933 "Strömungsgesetze in rauhen Röhren" in *Forschungsheft 361, Teil B*. VDI Verlag, Berlin.
- OURIEMI, M., AUSSILLOUS, P., MEDALE, M., PEYSSON, Y. & GUAZZELLI, É 2007 Determination of the critical Shields number for particle erosion in laminar flow. *Physics of Fluids* **19** (6), 061706.
- PÄHTZ, T., CHEN, Y., ZHU, R., THOLEN, K. & HE, Z. 2026 Coarse-graining particulate two-phase flow. *Granular Matter* **28**, 20.
- PÄHTZ, T., CLARK, A. H., VALYRAKIS, M. & DURÁN, O. 2020 The physics of sediment transport initiation, cessation, and entrainment across aeolian and fluvial environments. *Reviews of Geophysics* **58** (1), e2019RG000679.
- PÄHTZ, T. & DURÁN, O. 2018a The cessation threshold of nonsuspended sediment transport across aeolian and fluvial environments. *Journal of Geophysical Research: Earth Surface* **123** (8), 1638–1666.
- PÄHTZ, T. & DURÁN, O. 2018b Universal friction law at granular solid-gas transition explains scaling of sediment transport load with excess fluid shear stress. *Physical Review Fluids* **3** (10), 104302.
- PÄHTZ, T. & DURÁN, O. 2020 Unification of aeolian and fluvial sediment transport rate from granular physics. *Physical Review Letters* **124** (16), 168001.
- PÄHTZ, T., LIU, Y., XIA, Y., HU, P., HE, Z. & THOLEN, K. 2021 Unified model of sediment transport threshold and rate across weak and intense subaqueous bedload, windblown sand, and windblown snow. *Journal of Geophysical Research: Earth Surface* **126** (4), e2020JF005859.
- POGGIALI, V., MASTROGIUSEPPE, M., HAYES, A. G., SEU, R., BIRCH, S. P. D., LORENZ, R., GRIMA, C. & HOFGARTNER, J. D. 2016 Liquid-filled canyons on titan. *Geophysical Research Letters* **43** (15), 7887–7894.
- REBAI, D., BERZI, D., BALLIO, F. & MATOUSEK, V. 2022 Experimental comparison of inclined flows with and without intense sediment transport: Flow resistance and surface elevation. *Journal of Hydraulic Engineering* **148** (12), 04022026.
- RECKING, A. 2010 A comparison between flume and field bed load transport data and consequences for surface-based bed load transport prediction. *Water Resources Research* **46** (3), W03518.
- SCHIEBER, JUERGEN 2016 Mud re-distribution in epicontinental basins – Exploring likely processes. *Marine and Petroleum Geology* **71**, 119–133.
- SHCHEPETKINA, ALINA, GINGRAS, MURRAY K., MÁNGANO, M. GABRIELA & BUATOIS, LUIS A. 2019 Fluvio-tidal transition zone: Terminology, sedimentological and ichnological characteristics, and significance. *Earth-Science Reviews* **192**, 214–235.
- SHI, P. & RZEHAKE, R. 2019 Lift forces on solid spherical particles in unbounded flows. *Chemical Engineering Science* **208**, 115145.
- SONG, T. 1994 Velocity and turbulence distribution in nonuniform and unsteady open-channel flow. PhD thesis, Swiss Federal Institute of Technology EPFL, Lausanne, Switzerland.
- SONG, T. & CHIEW, Y. M. 2001 Turbulence measurement in non-uniform open-channel flow using acoustic Doppler velocimeter (ADV). *Journal of Engineering Mechanics* **127** (3), 219–232.

- SUN, R., XIAO, H. & SUN, H. 2017 Realistic representation of grain shapes in CFD-DEM simulations of sediment transport with a bonded-sphere approach. *Advances in Water Resources* **107**, 421–438.
- TENNEKES, H. & LUMLEY, J. L. 1972 *A First Course in Turbulence*. MIT Press, Cambridge, MA.
- VANONI, V. A. & BROOKS, N. H. 1957 *Laboratory studies of the roughness and suspended load of alluvial streams*. California Institute of Technology, Pasadena, CA, Report E-68.
- WIBERG, P. L. & SMITH, J. D. 1987 Calculations of the critical shear stress for motion of uniform and heterogeneous sediments. *Water Resources Research* **23** (8), 1471–1480.
- XIE, J., HU, P., PÄHTZ, T., HE, Z. & CHENG, N. 2022 Fluid-particle interaction regimes during the evolution of turbidity currents from a coupled les/dem model. *Advances in Water Resources* **163**, 104171.
- YAGER, E. M., VENDITTI, J. G., SMITH, H. J. & SCHMEECKLE, M. W. 2018 The trouble with shear stress. *Geomorphology* **323**, 41–50.
- YANG, S. Q., LIM, S. Y. & MCCORQUODALE, J. A. 2005 Investigation of near wall velocity in 3-d smooth channel flows. *Journal of Hydraulic Research* **43** (2), 149–157.
- YANG, X. I. A., PARK, G. ILHWAN & MOIN, P. 2017 Log-layer mismatch and modeling of the fluctuating wall stress in wall-modeled large-eddy simulations. *Physical Review Fluids* **2** (10), 104601.
- ZHANG, Q., DEAL, E., PERRON, J. TAYLOR, VENDITTI, J. G., BENAVIDES, S. J., RUSHLOW, M. & KAMRIN, K. 2022 Fluid-driven transport of round sediment particles: From discrete simulations to continuum modeling. *Journal of Geophysical Research: Earth Surface* **127** (7), e2021JF006504.
- ZHANG, Q., DEAL, E., PERRON, J. TAYLOR, VENDITTI, J. G., BENAVIDES, S. J., RUSHLOW, M. & KAMRIN, K. 2025 Discrete simulations of fluid-driven transport of naturally shaped sediment particles. *Journal of Geophysical Research: Earth Surface* **130** (5), e2024JF007937.
- ZHU, R., CHEN, Y., PÄHTZ, T., THOLEN, K. & HE, Z. 2026 On buoyancy in disperse two-phase flow and its impact on well-posedness of two-fluid models. <https://doi.org/10.48550/arXiv.2507.21602> .